

Laser Absorption Chemical Species Tomography

by

Matthew G. Twynstra

A thesis
presented to the University of Waterloo
in the fulfilment of the
thesis requirement for the degree of
Master of Applied Science
in
Mechanical Engineering

Waterloo, Ontario, Canada, 2013

© Matthew G. Twynstra 2013

AUTHOR'S DECLARATION

I hereby declare that I am the sole author of this thesis. This is a true copy of the thesis, including any required final revisions, as accepted by my examiners.

I understand that my thesis may be made electronically available to the public.

ABSTRACT

Recent advancements in optics and photonics have led to the development of laser absorption spectroscopy tomography as an emerging technology for mapping the planar distribution of chemical species concentrations for various applications. In typical implementations of the method, the discretization required to achieve a reasonable level of spatial resolution of the reconstructed image and the high cost of experimental equipment creates a limited data tomography problem in which the measurements alone are not sufficient to specify a unique reconstruction. Therefore, reconstruction algorithms must incorporate additional information that promotes presumed physical attributes of the concentration distribution.

This thesis outlines two advancements in the field of limited data absorption tomography. First, a novel reconstruction algorithm integrating the use of level set methods is presented that incorporates the additional *a priori* knowledge of a distinct interface between the species of interest and co-flow. The added *a priori* further reduces the ill-posedness of the system to produce a final concentration distribution that explains the laser absorption measurements and is qualitatively consistent with advection/diffusion transport. The algorithm is demonstrated by solving a simulated laser tomography experiment on a turbulent methane plume, and is compared with the current state-of-the-art reconstruction algorithm.

Given the limited number of attenuated measurements, accurate reconstructions are also highly dependent on the locations sampled by the measurement array. This thesis displays how the mathematical properties of the coefficient matrix, \mathbf{A} , formed by the locations of the lasers, are related to the information content of the attenuation data using a Tikhonov reconstruction framework. This formulation, in turn, becomes a basis for a beam arrangement design algorithm that minimizes the reliance on additional assumed information about the concentration distribution. Using genetic algorithms, beam arrangements can be optimized for a given application by incorporating physical constraints of the beam locations. The algorithm is demonstrated by optimizing unconstrained and constrained arrangements of light sources and detectors. Simulated experiments are performed to validate the optimality of the arrangements.

ACKNOWLEDGEMENTS

I would first like to thank my supervisor, Kyle Daun, for his help and guidance throughout my Masters research. His help and direction during my time at the University of Waterloo has been a great support for this thesis and other works we have published together. I am extremely grateful for his time and effort, teaching in more ways than one how to carry myself as a researcher and engineer.

I would also like to thank my friends and fellow graduate students Tim Sipkens, Farzan Memarian, Jeff Labahn and Dominic Ma for their help during my studies and for making my time at UW more enjoyable.

I would like to thank Kate Howard for her tremendous support, patience and understanding during my research. It did not go unnoticed and I am thankful for at least trying to show interest in work that sometimes seems abstract.

Finally, I would like to thank my parents, Brian and Kim Twynstra, who always made me believe that with hard work I could accomplish anything I wanted. Without their support I would not have been able to accomplish any of my goals.

TABLE OF CONTENTS

LIST OF FIGURES	VII
LIST OF TABLES	IX
NOMENCLATURE	X
SUBSCRIPTS AND SUPERSSCRIPTS	X
1. INTRODUCTION	1
1.1 Motivation.....	1
1.2 Available Technologies.....	1
1.3 Thesis Outline	3
2. LITERATURE REVIEW	5
2.1 Laser Absorption Chemical Species Tomography Overview	5
2.2 Spectroscopy	6
2.3 Reconstructions and Inverse Theory	11
2.4 Full-Rank and Limited Data Tomography	13
2.5 Reconstruction Algorithms	15
2.5.1 One-Dimensional Tomographic Reconstructions	16
2.5.2 Two-Dimensional Tomographic Reconstructions	18
2.5.2.1 Frequency-Based Reconstruction Algorithms	18
2.5.2.2 Algebraic Reconstruction Algorithms	20
2.5.2.2.1 Landweber Iterative Methods	21
2.5.2.2.2 Tikhonov Regularization Methods.....	24
3. LEVEL SET METHODS AND RECONSRUCTION ALGORITHMS.....	28
3.1 Tomography Priors for Turbulent Plumes and Jets.....	28
3.2 Level Set Method Overview	31
3.3 Application of LSM to Linear Inverse Theory.....	33
3.4 Level Set Evolution Regularization	34
3.5 Extension to laser absorption chemical species tomography	36
3.6 Results and Discussion.....	40
3.6.1 Heuristics	41
3.6.2 Results	42
4. ABSORPTION TOMOGRAPHY DETECTION ARRAY OPTIMZATION.....	46
4.1 Beam Arrangement and Reconstruction Accuracy	46
4.2 Resolution Matrices	49
4.2.1 Resolution Matrices for Limited-Data Tomography.....	50
4.3 Parameter Selection.....	52
4.4 Validation of Fitness Function	54
4.5 Genetic Algorithms and Beam Arrangement Optimization	56
4.6 Effects of Beam Misalignment.....	62
4.7 Effect of Number of Beams on Reconstruction Accuracy	63
4.8 Constrained Arrangement Optimization for FLITES Project	65
5. CONCLUSIONS AND FUTURE WORK.....	72
5.1 Conclusions.....	72
5.2 Future Work	73
5.2.1 Level Set Method Algorithm Parameters and Initial Conditions	73
5.2.2 Resolution Matrices and Optimization.....	74

6. REFERENCES.....75

LIST OF FIGURES

Figure 1.1 – Planar Laser Induced Fluorescence General Experimental Setup	2
Figure 2.1 – Laser Absorption Tomography General Experimental Setup.....	5
Figure 2.2 – Geometry of Beam Transecting Tomography Field	6
Figure 2.3 – Absorption Spectrum of Various Gases at STP (T=296K, P=1 atm)	8
Figure 2.4 – Continuous Broadened Absorption Spectrum for Various Gases (T=296K, P=100 atm)	9
Figure 2.5 – Discretized Reconstruction Domain and Ray-Sum Geometry	12
Figure 2.6 – (a) Singular values from A matrix corresponding to beam arrangement in (b), 1600 pixel reconstruction domain.....	15
Figure 2.7 – Sample one-dimensional onion-peeling reconstruction domain and discretization	16
Figure 2.8 – Singular values of A_{OP} matrix from one-dimensional axisymmetric problem	17
Figure 3.1 – (a) Spreading of a turbulent round jet, (b) Mass transport terms.....	30
Figure 3.2 – Classical level set geometry (a) sample level set function; (b) corresponding implicit X-domain via Equation (3.1).....	32
Figure 3.3 – Continuous domain level set geometry (a) sample level set function; (b) corresponding implicit X-domain via Equation (3.15).....	37
Figure 3.4 – (a) Initialization of ϕ as SDF; (b) Irregular level set function after non-regularized evolution with level set, Γ , shown in white.....	38
Figure 3.5 – Large eddy simulation of mixed buoyant methane plume.....	41
Figure 3.6 – Singular values of A matrix vs. λ for 1600 pixel domain.....	42
Figure 3.7 – Sample LSM and Tikhonov reconstructions: (a-c) $t = 80s$, (d-f) $t = 100s$, Zero level set, Γ shown in red.....	43
Figure 3.8 – Instantaneous and average reconstruction error results for Tikhonov and LSM algorithms ..	44
Figure 4.1 – Sample results of simulated experiment using beam arrangement in Figure 4.2 (d), with tiled phantom from (a) shown in (c), corresponding reconstructions (b) and (d) (Figure adopted from Wright et al. 2005)	47
Figure 4.2 – Sample beam arrangements: (a) orthogonal, rectilinear 32 beam, (b) 3-projection fan 33 beam, (c) Irregular 27 beam, (d) Irregular 32 beam.....	47
Figure 4.3 – Radon plot for beam arrangement Figure 4.2 (c)	48
Figure 4.4 – Contour plots of resolution matrices corresponding to Figure 4.2 (a) and (d) for Figure 4.2 (a) and (b) respectively, 1600 pixel reconstruction domain	52
Figure 4.5 – (a) Sample Gaussian phantom, (b) Corresponding Tikhonov reconstruction and error	53
Figure 4.6 – Reconstruction error for various values of λ , using random Gaussian phantoms, 1600 pixel domain, beam arrangement 4.2 (a).....	54
Figure 4.7 – Fitness function and reconstruction error for regular beam arrangement for various beam spacings	55
Figure 4.8 – Fitness function and reconstruction error for fan beam arrangement with various values of spread angle	56
Figure 4.9 – General genetic algorithm flow chart	57
Figure 4.10 – (a) Genetic algorithm progression for 32 beam optimization, (b) Unconstrained GA optimized 32- beam arrangement.....	59
Figure 4.11 – Error and normalized fitness comparison of beam arrangements using random Gaussian phantoms	60
Figure 4.12 - Error and normalized fitness comparison of beam arrangements using LES phantom.....	61
Figure 4.13 – Sample LES phantom and reconstructed concentration profiles for various beam arrangements: (b) for Figure 4.2 (a), (c) for Figure 4.2 (b), (d) for Figure 4.2 (c), (e) for Figure 4.2 (d), and (e) Figure 4.10.....	62
Figure 4.14 – Normalized fitness and error for various values of m using random Gaussian phantoms....	64
Figure 4.15 – FLITES geometric arrangement of engine and beam arrangement mounting fixture (Figure adopted from McCormick 2013).....	66

Figure 4.16 - Reconstruction results and corresponding error for each optimized case	69
Figure 4.17 – Fitness and reconstruction error for each optimization case.....	69
Figure 4.18 – Genetic algorithm progressions and optimized beam array for each optimization case.....	71

LIST OF TABLES

Table 4.1 – Number of beam, fitness, normalized fitness, and average error using random Gaussian phantoms for various beam arrangements	59
Table 4.2 – Number of beam, fitness, normalized fitness, and average error using LES phantom for various beam arrangements.....	61
Table 4.3 – Average reconstruction error for original and misaligned beam arrangements using random Gaussian phantoms	63
Table 4.4 – FLITES optimization cases and corresponding constraints	67

NOMENCLATURE

$\mathbf{A}(\Phi)$	Algebraic reconstruction kernel
$\mathbf{A}^\#$	Kernel generalized inverse
\mathbf{b}	Laser attenuation data
E	Level set energy
$\mathbf{F}(\Phi)$	Fitness function
\mathbf{F}	Level set velocity matrix
$I_{\eta 0}$	Initial laser intensity
I_η	Attenuated laser intensity
\mathbf{L}	Tikhonov smoothing matrix
m	Number of beams in reconstruction
n	Number of pixels used in reconstruction
$\mathbf{R}(\Phi)$	Resolution matrix
$R(\phi)$	Level set regularization term
$R^{(s,\theta)}$	Radon Space
s	Perpendicular distance between beam and origin
u	Parametric distance along beam
X	Level set method implicit domain
\mathbf{x}	Target species concentration profile
\mathbf{x}_λ	Reconstructed solution
\mathbf{x}^{exact}	Exact solution
$\delta \mathbf{x}$	Discrepancy between exact and reconstructed solutions
ε	Reconstruction error
θ	Angle formed between beam and vertical axis
κ_η	Spectral absorption coefficient
λ	Regularization parameter
Φ_i	i th pair of $[s, \theta]^T$ values
Φ	m-dimension vector of Φ_i
ϕ	Level set function

SUBSCRIPTS AND SUPERSSCRIPTS

$*$	Optimal solution
int	Internal
ext	External
LS	Least squares solution
η	Wavenumber
n	Nullspace
k	k th iteration

1. INTRODUCTION

1.1 Motivation

The operation and efficiency of many industrial devices is highly influenced by chemical reactions dependent on factors such as mixture homogeneity or distribution. Advanced knowledge of chemical species location and concentration is paramount when optimizing such chemical processes as fuel combustion and neutralization reactions of certain harmful species. For example, the performance, efficiency and emissions of internal combustion engines depend strongly on obtaining controlled fuel-air dispersion within the combustion chamber (Wright 2005, 2010). Likewise, accurately measuring and mapping the exhaust species produced from experimental aerospace engines allows detection of defective burners and components (McCormick 2013). Therefore, design optimization and performance diagnostics of such devices is highly influenced by the ability to modify measure and map such properties. Similarly, accurate emission detection is essential to avoid the problem of “ammonia slip” from selective catalytic and noncatalytic reduction systems in power plants (Javed 2007).

Applications like those mentioned create a pressing need for a diagnostic that can provide real-time concentration distributions and measurement of gas species to pinpoint potential problems and improve the future performance of these devices.

1.2 Available Technologies

The oldest technology for measuring gas concentration distributions is physical probing. Though measuring concentration through physical probing is simple to implement, the method has a number of drawbacks (Eckbreth 1988). First, physical probes can only provide a single point or average measurement for an area with limited temporal and spatial resolution, requiring many measurements to accurately sample the flow distribution. Second, the presence of the probe within the flow itself will also perturb the flow itself resulting in inaccurate measurements. Last, in many applications gaining physical

access to the flow field is very difficult, for example, measuring combustion emissions within an automotive engine (Wright 2005).

One technology that overcomes the drawbacks of physical measurements is planar laser-induced fluorescence (PLIF). PLIF relies on the spectrally selective fluorescent properties of materials to provide real-time flow time visualization and species distribution analysis of the flow field. PLIF is non-invasive species mapping technique that also has temperature, velocity, pressure and density measurement capabilities (Hanson 1990). In the general arrangement, a flow field often containing a dopant (e.g. OH^\cdot) is traversed by a laser sheet from pulsed, tunable laser source. Under specific conditions, the laser light excites the dopant causing it to fluoresce.

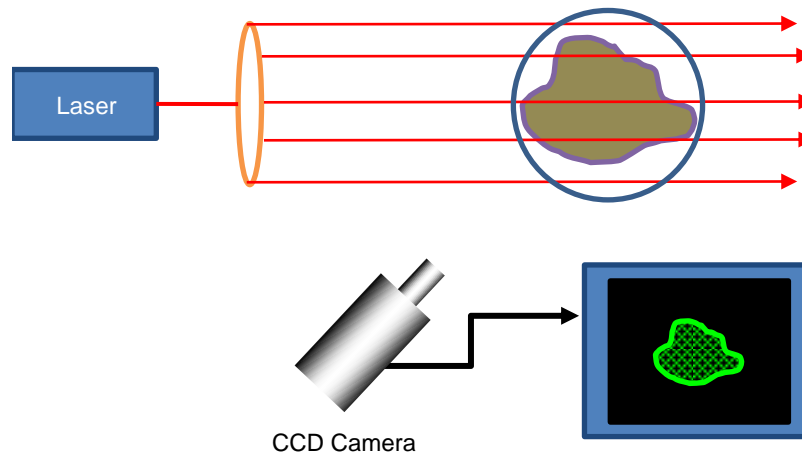


Figure 1.1 – Planar Laser Induced Fluorescence General Experimental Setup

The fluorescence is recorded using a detector camera from a second optical plane, typically perpendicular to the laser sheet, as shown in Figure 1.1. The detector typically uses a narrow-band filter to capture a specific band of the fluorescent emittance to observe specific phenomena. The camera is typically a solid-state CCD array which allows for excellent flow visualization with detection arrays consisting of over one million elements (Hanson 1990). The fluorescent intensity recorded by the detector can then be related to various properties of the flow, particularly species concentration. The high spatial resolution of PLIF makes it particularly useful in the study of turbulent flows and combustion theory (Cessou 2000, Hanson 1990).

Though PLIF has been successfully implemented in industry for process monitoring and diagnostics, the method has several limitations. First, the flow field must contain a chemical species with resonant wavelengths accessible to the laser; otherwise a fluorescent tracer must be added to dope the target species. This, in turn, can lead to measurement error as complete mixing between the target species and tracer may not always occur. More problematic is the requirement of a second optical access plane (Carey 2000, Hindle 2001). When using PLIF in engine diagnostics, for example, costly modifications must be made to the engine in order to accommodate the detection plane.

This thesis presents design and computational advancements in the methods of laser absorption spectroscopic tomography, an emerging alternative in applications of gaseous species measurement and mapping that avoids the limitations of other technologies. Laser absorption spectroscopic tomography is a line of sight detection technique that uses a set of attenuation measurements through the flow field. Using the geometric location and attenuation measurement of each laser, the concentration distribution of the species can be reconstructed. However, since a limited number of measurements can be made relative to the number of unknown variables, the reconstructions must incorporate traits of the expected species distribution in order to specify a unique solution. The difficulty in producing a physical and accurate solution is then related to this prior knowledge as well as the manner in which they are applied to the problem physics. Additionally, since the number of attenuation measurements is fixed and finite, proper arrangement of the beams has a pronounced effect on the accuracy of the reconstructions.

The main contributions of this work to the field of laser absorption spectroscopic tomography are: (1) the design of a new tomographic reconstruction algorithm incorporating novel *a priori* information into the rank-deficient problem and (2) a novel method for the detection array arrangement optimization to maximize spatial resolution and minimize measurement error of the system.

1.3 Thesis Outline

This thesis is divided into five main sections; an extended literature review on the methodology and principals of laser absorption tomographic reconstruction and spectroscopy, presentation of the

application of the level set method to tomographic gaseous flow reconstruction algorithms with discussion of implementation and results, investigation and optimization of absorption tomography detection arrangements using resolution matrices, and a summary of the presented work with conclusions.

Chapter 2 will first present the general methodology of traditional laser absorption tomography experiments and implementations. A brief discussion on the underlying spectroscopic principals of absorption tomography will follow. Next, the underlying mathematical principals on tomography reconstructions and inverse theory will be presented with examples of reconstruction algorithms in published literature.

Chapter 3 will focus on the design of a novel tomographic reconstruction algorithm for gaseous flows by integrating the use of level set methods. The use of *a priori* information from published literature will be examined and the possibility of additionally incorporating a distinct interface between the species of interest and surrounding fluid into the reconstruction method will be discussed. An overview of the level set method will then be presented with modifications for use inverse problems and continuously varying fields. Sample reconstructions and comparison to alternate reconstruction methods will be examined and discussed.

Chapter 4 focuses on how the light sources and detectors should be arranged to maximize reconstruction accuracy. The concept of resolution matrices will be presented and their derivation regarding how they relate to reconstruction error of tomographic experiments will be shown. The use of genetic algorithms and resolution matrices to optimize detection arrangements will then be conducted with quantitative comparison between an optimized arrangement and others used in previous studies.

Last, Chapter 5 will summarize the work presented and how the advancements from this work will impact the field of laser absorption tomography. Recommendations of future work and extensions will also be discussed.

2. LITERATURE REVIEW

2.1 Laser Absorption Chemical Species Tomography Overview

Laser absorption chemical species tomography (CST) is an emerging technology for the measurement and mapping of gaseous species that overcomes limitations of physical probing and PLIF methods. In this procedure a number of line-of-sight laser attenuation measurements are made through the flow field. From the set of discrete attenuation measurements, the unknown species concentration is then tomographically reconstructed.

The general experimental setup is shown in Figure 2.1. A set of m lasers and detector pairs are arranged as a planar array perpendicular to the flow. The laser can either traverse the flow field directly or through some optical containment medium that permits the transmission of light at the source's waveband. In many arrangements, one laser signal is diverted from the flow field for use a reference signal of the source.

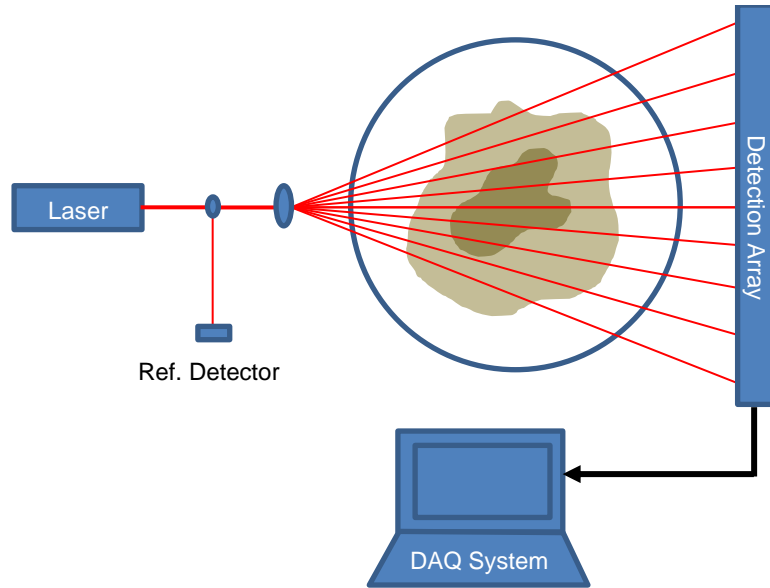


Figure 2.1 – Laser Absorption Tomography General Experimental Setup

The attenuation of the i^{th} laser beam transecting a participating medium is governed by the Beer-Lambert law (Daun 2010, Garcia Stewart 2003, Modest 2003, Ma 2013, Wright 2005, 2010),

$$\ln \frac{I_{\eta 0,i}}{I_{\eta,i}} = b(\Phi_i) = \int_0^\infty \kappa_\eta [\mathbf{r}_{\Phi_i}(u)] du \quad (2.1)$$

where $I_{\eta 0,i}$ and $I_{\eta,i}$ are the incident and exiting intensities respectively, η is the wavenumber of light, $\mathbf{r}_{\Phi_i}(u)$ is the position vector, κ_η is the spectral absorption coefficient of the flow species, and u is a parametric distance along the beam. The attenuation model neglects the effect of scattering since the molecular scattering cross-section is much smaller than the absorption cross-section at mid-IR wavelengths (Modest 2003). The position of each beam is specified by $\Phi_i = [s_i, \theta_i]^T$, where s_i is the perpendicular distance from the laser beam to the origin of the flow field, and θ_i is the angle formed between the beam and the flow field y-axis, as seen in Figure 2.2.

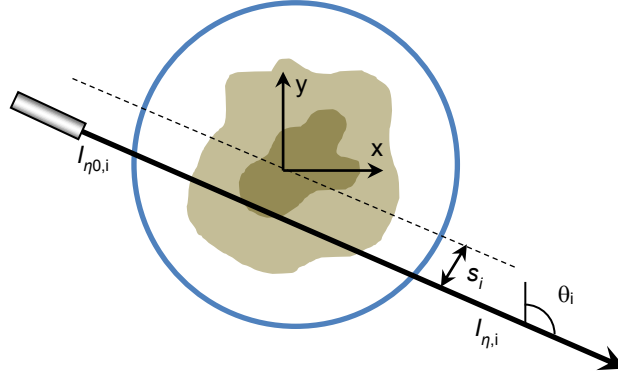


Figure 2.2 – Geometry of Beam Transecting Tomography Field

The detector measurement for each beam is simultaneously recorded using a data acquisition (DAQ) system as seen in Figure 2.1. Using the reference signal measurement, the attenuation for each beam can be calculated using Equation (2.1), forming a vector of m attenuation measurements.

2.2 Spectroscopy

Laser absorption tomography relies heavily on the application of spectroscopic principals. Spectroscopy is the study of interaction of radiated energy and matter, particularly the wavelength dependence of this interaction. In the context of chemical species laser absorption tomography, we are

primarily concerned with the spectral absorption properties of molecular gases which exhibit significant absorption in very specific and limited regions of the spectrum (Klingbeil 2006).

The absorption coefficient for each beam can be inferred using Equation (2.1), and then used to computed to concentration of the species of interest. The absorption coefficient, κ_η , scales with the mole fraction of the absorbing species, $\chi(\mathbf{r})$, through

$$\kappa_\eta = \sigma_\eta N = \sigma_\eta \frac{\chi(\mathbf{r})P}{R^\circ T} \quad (2.2)$$

where σ_η is the spectral molecular absorption cross-section, N is molecular number density, P and T are the pressure and temperature of the gas mixture, assumed to be uniform, and R° is the universal gas constant. The molecular absorption cross-section can either be found from tabulated data, such as the HITRAN database (Rothman 2009), or by performing absorption experiments on a test cell containing a known concentration (Carey 1999, Klingbeil 2006).

An example absorption spectrum for methane, carbon monoxide and water vapor at 296 K at 1 atm is shown in Figure 2.3. From this figure it is shown that for these gases there are absorption windows that indicate that for certain wavelengths of radiation, there is nearly full transmittance of the source through a cross-section of gases, regardless of the gas concentration. These absorption lines exist due to the specific rotational and vibrational quantized energy levels that characterize a molecule. The magnitude of a photon's energy levels is directly related the frequency of the photon energy, scaled by Planck's constant, $E = h\nu$, where h is Planck's constant, 6.626×10^{-34} J·s and ν is frequency of the photon. When a gas molecule encounters light possessing energy that exactly corresponds to the transition between two of the molecule's quantized energy levels, the light is absorbed by the molecule. This type of absorption between a molecule's bound energy states is referred to as "bound-bound" absorption is by far the most common in gases of moderate temperatures, i.e. $T_{\text{gas}} < 500$ K, and thus is of the most interest in absorption spectroscopy applications. Because of the strong absorption characteristics of many gases in the region, as well as the availability of detectors and light sources in this spectral region, laser

absorption experiments are typically interested in the IR and near-IR regions of the emission spectrum (Carey et al 1999, Porter 2009).

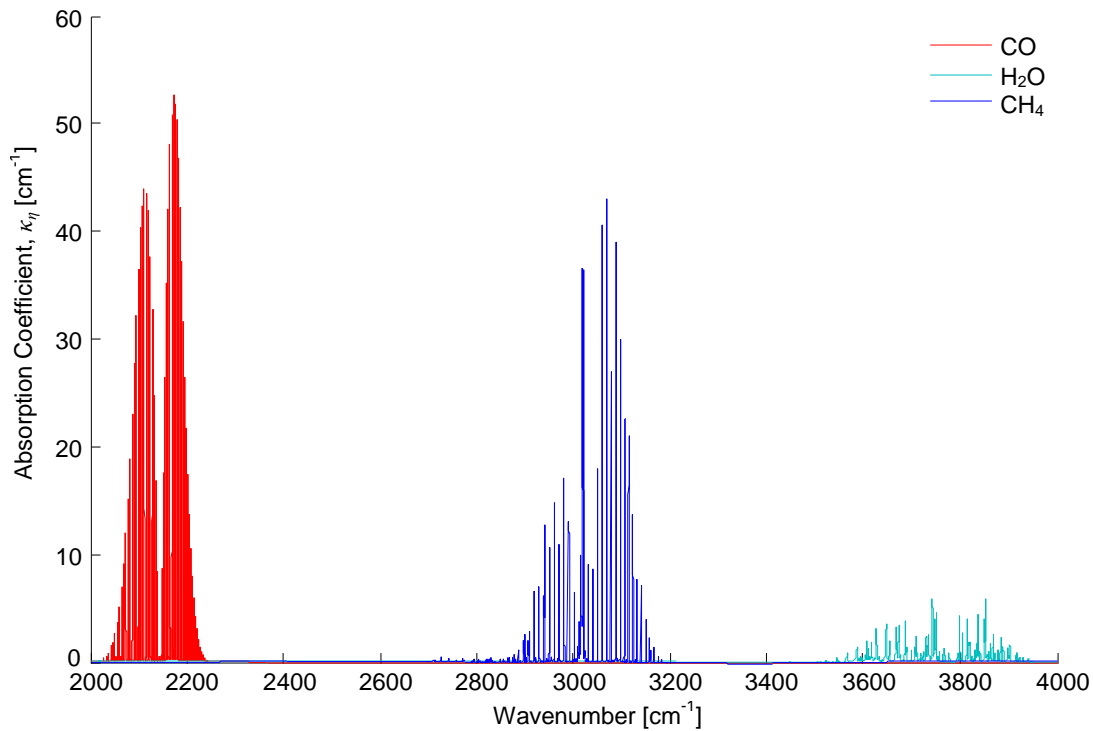


Figure 2.3 – Absorption Spectrum of Various Gases at STP (T=296K, P=1 atm)

Though theoretically absorption occurs and infinitesimally thin absorption lines as depicted in Figure 2.3, typically the spectral absorption lines are broadened, resulting in a band-like absorption structure as shown in Figure 2.4. Broadening and shifting of a gas' absorption spectral lines occurs due to several physical mechanisms, most notably; natural broadening, Doppler broadening, Stark broadening, and collision broadening.

Collision broadening accounts for molecular collisions within the gas that result in modified energy states of the gas molecules. Increased collision rates thus create uncertainty in the energy states of the gas resulting in broadening of the spectral lines. The effects of collision broadening can be approximated using kinetic theory of gases. The collision rate of a gas is directly related to the gas pressure and thus the broadening width of a spectral line is linearly affected by pressure. The collision broadening of is a symmetric Lorentzian profile. In the field of gas absorption tomography, collision

broadening is by far the most pronounced mechanism of broadening, particularly in the infra-red range, and thus requires the most consideration.

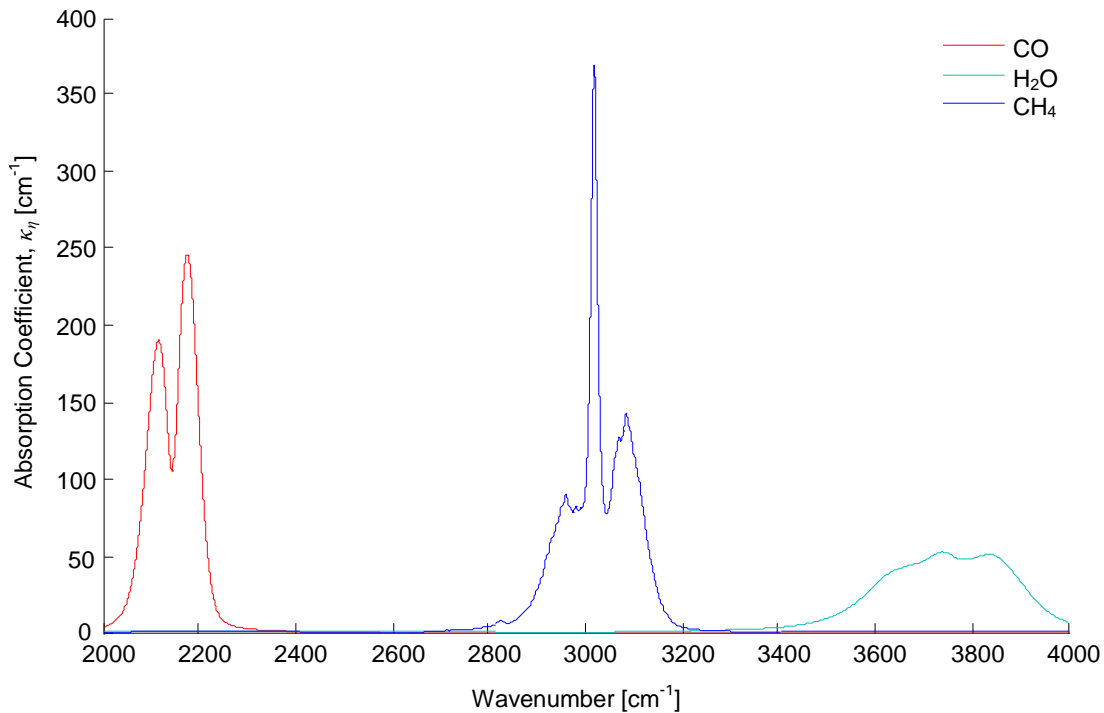


Figure 2.4 – Continuous Broadened Absorption Spectrum for Various Gases (T=296K, P=100 atm)

In laser absorption tomography, spectroscopy is used to infer the species concentration from an absorption measurement. Spectroscopic analysis is also used to find the wavelengths at which the target species strongly absorbs. Additionally, other chemical species in the flow may also exhibit absorption in the chosen wavelength region. Thus, the absorption spectrum of all gaseous chemical species within the flow field must be considered to avoid overlapping absorption bands that can account for inaccurate measurement of the species of interest. The wavelength selection of the source must also incorporate the consideration of the maximum species concentration expected as well as the strength of the laser source intensity. If a wavelength is chosen that corresponds to very high levels of absorption, the source intensity may be such that all incident radiation is absorbed during attenuation, resulting in a non-existent exit intensity, and thus inadequate data to infer the species concentration along the beam's path. Conversely, if an absorption band is identified and chosen by the source with very little absorption with

respect to the expected gas concentrations to be measured, the amount of absorbed intensity may be negligible with respect to the noise of the detection system.

Because of their ability to achieve a wide range of wavelengths with relatively high signal strengths, tunable diode lasers (TDLs) are a common choice for as a laser source in absorption tomography experiments. The tunability of the laser means that the laser absorption experiments can be conducted on several different species of the flow field to measure and map gas concentrations. Tunable diode lasers can also be used in wavelength sweeping modes that allow full transmission across an absorption band of a species to effectively measure the broadening of a spectral line to infer such variables as pressure and temperature as well as species concentration. The high intensity of TDLs also means that a single source's signal can be split into many measurement paths using beam splitting optics. Laser sources can be subject to signal drift over time, modifying the value of the reference signal for each source, a factor that is avoided using a single source split into several beams. In monochromatic applications, a common source technology is Helium-Neon (HeNe) lasers. HeNe source are commonly used because of their low cost, high durability and the strong absorption of the 3.39 μm wavelength by hydrocarbons and methane gas (Edwards 1965, Klingbeil 2006, Porter 2009).

In single wavelength applications, precautions are usually taken to minimize the linewidth of the laser to achieve a very specific interaction between the source and the absorption band of the species. The narrowing of the source's emission is typically accomplished using spectrally selective materials and narrow-band filters. This narrow linewidth negates the incorporation of band-averaging models for the species absorption and allows for much more certainty in the concentration measurement of a beam.

The choice of source emission wavelength also defines the required measurement range of the detection system and additional optics. The choice of detection technology is done by maximizing the detectability in the source's emission range and minimizing the signal-to-noise ratio (SNR) of the detection signal, thereby decreasing the detectability limit of the experiment. To avoid the detection of intensity due to the emission of radiation by the flow field, a narrow-band filter is also utilized at the on the detection system to achieve a very specific spectral measurement unique to the source attenuation.

2.3 Reconstructions and Inverse Theory

While a single LOSA measurement can determine the total number of molecules along the beam through Equation (2.2), a single beam cannot localize the distribution of the species. Using a set of m attenuation measurements each at different paths through the flow field, the goal of laser absorption tomography is to use all measurements simultaneously to solve the concentration profile of the gas species that describes the measurements obtained.

Equation (2.1) is a Fredholm integral equation of the first kind. Deconvolving this equation for the local absorption coefficient, $\kappa_\eta[\mathbf{r}]$, is mathematically ill-posed (Daun 2010, Verhoeven 1993, Wing 1991). Ill-posed problems arise from Hadamard's criteria for well-posed problems which state that (i) a solution exists, (ii) the solution is unique and (iii) the solution is robust to small changes in the measurement data (Hadamard 1923, Hansen 2002). Deconvolving Equation (2.1) is therefore ill-posed because it violates Hadamard's second criteria of uniqueness since an infinite set of candidate gas distributions exists that could be substituted into the integral to produce the observed attenuation data.

Reconstructions and discretization of the domain is accomplished using the Algebraic Reconstruction Technique (ART), linear algebra techniques and inverse theory. The algebraic reconstruction technique discretizes the flow field cross-section (i.e. gas distribution domain) into a set of n pixels. In this formulation each of the discretized pixels is assumed to obtain a uniform concentration of the target species. Though discretizing the domain creates some discretization error, it can be reduced by additional pixels at the expense of computational cost and increased ambiguity of the system.

Typically, the domain is segmented into a square grid of size $\sqrt{n} \times \sqrt{n}$, as shown in Figure 2.5. Using this discretization, the attenuation measurement for each beam, b_i , from the integral in Equation (2.1) can be approximated using a "ray-sum" series,

$$b_i = \sum_{j=1}^n A_{ij} x_j \quad (2.3)$$

where A_{ij} is the chord length of the i^{th} beam subtended by the j^{th} pixel and x_j is the mole fraction-normalized absorption coefficient for the j^{th} pixel. A description of the terms in Equation (2.3) is

illustrated in Figure 2.5 for a single beam. Approximation of each attenuation measurement using Equation (2.3) for all m beams results in an $m \times n$ matrix equation,

$$\mathbf{Ax} = \mathbf{b} \quad (2.4)$$

where $\mathbf{A} \in \mathbb{R}^{m \times n}$ is a matrix containing the chord length of each laser beam through subtended by each of the n discretized pixels, $\mathbf{x} \in \mathbb{R}^n$ is a vector containing the target species concentration of each pixel, and $\mathbf{b} \in \mathbb{R}^m$ is a vector containing each attenuation measurement described by Equation (2.1).

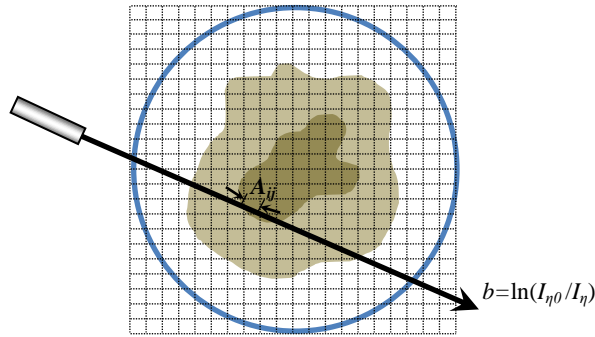


Figure 2.5 – Discretized Reconstruction Domain and Ray-Sum Geometry

Given enough attenuation measurements through the flow where each of the n pixels is sampled via an attenuation measurement, the flow field concentration distribution \mathbf{x} can be uniquely specified using least squares minimization of $\|\mathbf{b} - \mathbf{Ax}\|$ or directly through matrix inversion, i.e. $\mathbf{x} = \mathbf{A}^{-1}\mathbf{b}$. Unfortunately this situation is rarely encountered. Though a relatively a high spatial resolution is used for imaging and measurement, far fewer laser measurements are used for reconstructions compared to the number of pixels ($m \ll n$) due to the high cost of required optics and detection/emission systems as well as geometric constraints around the flow field. The rank-nullity theorem states that maximum rank of \mathbf{A} is m , and thus the large discrepancy between the number of unknowns and measurements creates a *limited data* tomography problem (Hansen 2002, Verhoeven 1993). Therefore, a unique concentration distribution cannot be specified through the measurements alone; additional information about the solution must be used to buttress the information contained in \mathbf{b} since Equation (2.4) is rank-deficient.

2.4 Full-Rank and Limited Data Tomography

In contrast to full-rank tomography where the domain of the problem is fully sampled (even over sampled in some cases), limited data tomography uses a relatively small number of measurements to reconstruct the variable distribution. Since some regions of the flow field are completely unsampled, there is no data to determine the unknown concentration profile in these areas. Mathematically, we state that a *limited data* tomography is represented by an underdetermined system of equations and as a consequence the \mathbf{A} matrix in Equation (2.4) contains a non-trivial null space. A reconstructed species distribution is then the sum of two components,

$$\mathbf{x} = \mathbf{x}^{\text{LS}} + \mathbf{x}^n \quad (2.5)$$

where the least squares component, $\mathbf{x}^{\text{LS}} = \text{argmin} (\|\mathbf{b} - \mathbf{A}\mathbf{x}\|)$, belongs to the range of \mathbf{A} , while the null component, \mathbf{x}^n , is a nontrivial vector belonging to the null space of the problem, $\{\mathbf{x}^n \in \mathcal{N}[\mathbf{A}]: \mathbf{x}^n \mathbf{A} \mathbf{x}^n = 0\}$.

The ill-posed or rank-deficient nature of an inverse problem can be visualized by carrying out a singular value decomposition of the kernel matrix, \mathbf{A} . Singular value decomposition (SVD) is method often used in signal processing used to determine the rank, range and nullspace of a matrix in addition to the system's stability to induced data noise. In SVD, the matrix $\mathbf{A} \in \mathbb{R}^{m \times n}$ is factored into

$$\mathbf{A} = \mathbf{U} \mathbf{\Sigma} \mathbf{V}^T = \sum_{i=1}^n u_i \sigma_i v_i^T \quad (2.6)$$

where $\mathbf{U} = (u_1, \dots, u_n) \in \mathbb{R}^{m \times n}$ and $\mathbf{V} = (v_1, \dots, v_n) \in \mathbb{R}^{n \times n}$ are matrices with orthonormal columns, i.e. $\mathbf{U}^T \mathbf{U} = \mathbf{V}^T \mathbf{V} = \mathbf{I}_n$, and $\mathbf{\Sigma} = \text{diag}(\sigma_1, \dots, \sigma_n)$ is an $n \times n$ diagonal non-negative matrix of decreasing order such that $\sigma_1 \geq \sigma_2 \geq \dots \geq \sigma_n \geq 0$ (Hansen 1990, 1992, 2002). The values of the $\mathbf{\Sigma}$ matrix are called the *singular values* of matrix \mathbf{A} . Because of the orthonormal nature of matrices \mathbf{U} and \mathbf{V} , SVD allows simple calculation of the kernel inverse,

$$\mathbf{A}^{-1} = \mathbf{V} \mathbf{\Sigma}^{-1} \mathbf{U}^T \quad (2.7)$$

and thus in a full-rank problem, i.e. $\text{Rank}[\mathbf{A}] = n$, a reconstructed solution can be acquired using SVD back-substitution,

$$\mathbf{x} = \sum_{i=1}^n \frac{u_i^T \mathbf{b}}{\sigma_i} \mathbf{v}_i \quad (2.8)$$

where u_j and v_j are the i^{th} column vectors of \mathbf{U} and \mathbf{V} and σ_j is the i^{th} singular value. Equation (2.8) illustrates the effect of small singular values on the reconstructed solution where very small perturbations in the vector \mathbf{b} are amplified via division by a small number, σ_i , which characterizes ill-posed problems that violate Hadamard's third criteria for well-posed problems. Unfortunately for rank-deficient problem such as that of limited data tomography, only m non-trivial singular values exist which results in the sum of Equation (2.8) only being evaluated for m terms before it is indeterminate, presenting a null space in the problem formulation. The SVD back-substitution for a rank-deficient problem is then

$$\mathbf{x} = \mathbf{x}^{LS} + \mathbf{x}^n = \sum_{i=1}^m \frac{u_i^T \mathbf{b}}{\sigma_i} \mathbf{v}_i + \sum_{j=1+m}^n C_j \mathbf{v}_j \quad (2.9)$$

which illustrates that there are an infinite set of vectors \mathbf{C} that can be substituted into Equation (2.9) that can explain the absorption data (Hansen 1990, 1992, 2002). Since there no unique solution for the reconstructed species distribution, the limited data tomography problem violates Hadamard's second criteria of uniqueness for well posed problems.

An example singular value plot for a limited data laser absorption tomography problem is shown in Figure 2.6. The parameters used for this sample problem are specified as $m = 32$, $n = 1600$ and the beam arrangement used to construct \mathbf{A} is shown in Figure 2.6 (b). From the plot we see the m non-trivial singular values that represent the rank of \mathbf{A} , i.e. $\text{Rank}[\mathbf{A}] = m$, and the $(n - m)$ null singular values that represent the null space of \mathbf{A} , i.e. $\text{Null}[\mathbf{A}] = (n - m)$.

To span the null space of a limited data, rank-deficient problem, it is necessary to supplement the measurement data with additional assumed attributes of the ideal solution. In a Bayesian context, these assumed attributes are called “priors” or *a priori* information, and correspond to the prior probabilities used to condition an indefinite likelihood function in Bayes' equation.

In laser absorption tomography, accurate reconstructions are founded on the definition and implementation priors that are physically sound. For the field of gaseous species tomography, the most

commonly used priors are non-negativity and spatial smoothness of the concentration distribution is often found in systems dominated by diffusion transport (Ma 2008).

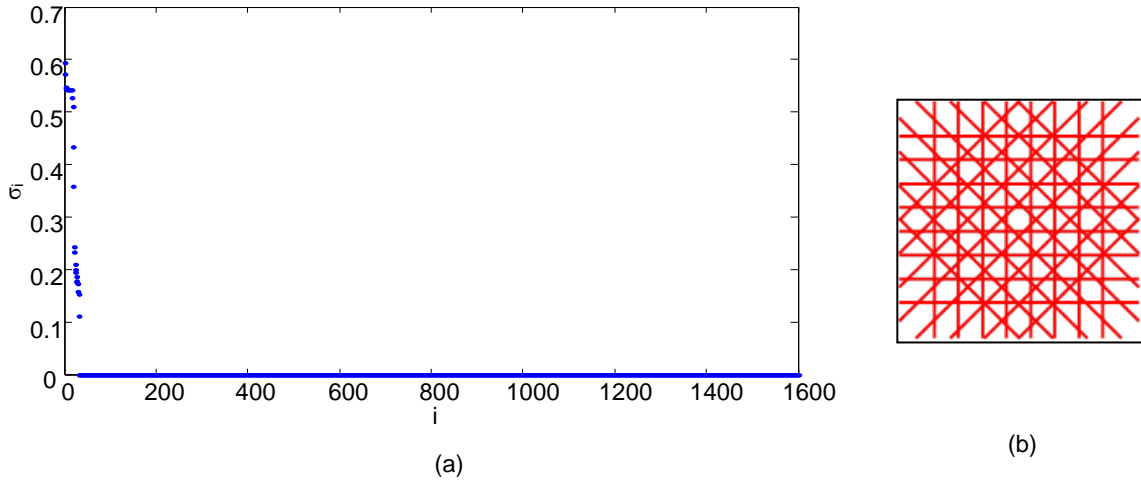


Figure 2.6 – (a) Singular values from A matrix corresponding to beam arrangement in (b), 1600 pixel reconstruction domain

The following section will present different implementations of reconstruction algorithms in literature including frequency and algebraic reconstruction techniques. Discussion will include how *a priori* information is used to supplement the experimental data as well as the relative advantages and disadvantages of each algorithm.

2.5 Reconstruction Algorithms

Incorporating line-of-sight measurements into a tomography reconstruction of spatially varying distributions has been approached by several different mathematical methods. Since the introduction of hard-field tomography, in which each detector is pair with only a single emitting source, two classes of reconstructions algorithms have emerged; frequency-based and algebraic-based reconstructions. Additionally, the domain can be discretized into either a one-dimensional or two-dimensional domain. Each class of algorithms is separated by the different mathematical basis to solving the species distribution.

2.5.1 One-Dimensional Tomographic Reconstructions

Solving the tomography on a one-dimensional domain imposes the additional constraint that the unknown species distribution is axisymmetric. This framework is commonly used by researchers because of the greatly reduced number of unknowns of the system, thereby reducing or eliminating the rank-deficiency of the system. An example axisymmetric domain is shown in Figure 2.7.

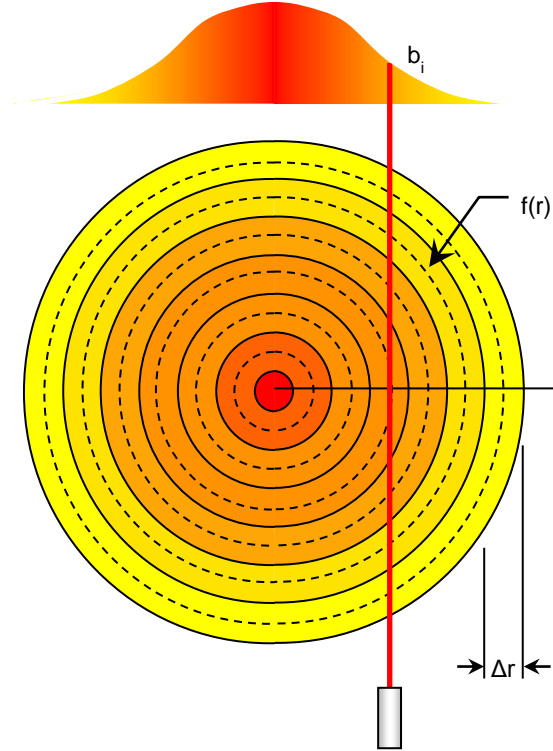


Figure 2.7 – Sample one-dimensional onion-peeling reconstruction domain and discretization

The axisymmetric tomographic reconstruction problem uses Abel integration equation

$$b = \ln \left(\frac{I_{\eta 0}}{I_{\eta}} \right) = 2 \int_x^R \frac{\mathbf{x}(r)r}{\sqrt{r^2 - x^2}} dr \quad (2.10)$$

where x is the abscissa coordinate of projected data, r is the radial coordinate of the property field, and R is the domain radius as shown in Figure 2.7 (Åkesson 2008). Through discretization of the domain using the onion-peeling (OP) method, as shown in Figure 2.7, each attenuation measurement, Equation (2.10), can be approximated using a series sum and the problem can be described by the matrix equation

$$\mathbf{A}_{OP}\mathbf{x}=\mathbf{b} \quad (2.11)$$

where \mathbf{b} is a set of attenuation measurements, \mathbf{x} is a set of species concentrations at each discretized annulus and \mathbf{A}_{OP} contains the geometric locations of the lasers. While Abel's integration equation satisfies the first two of Hadamard's criteria for well-posed problems, i.e. a unique solution can be mathematically found, the system is still defined as discrete ill-posed since the reconstruction is highly sensitive to small perturbation in the attenuation data due to the small singular values of the kernel, \mathbf{A}_{OP} , which vary over orders of magnitude, as shown in Figure 2.8.

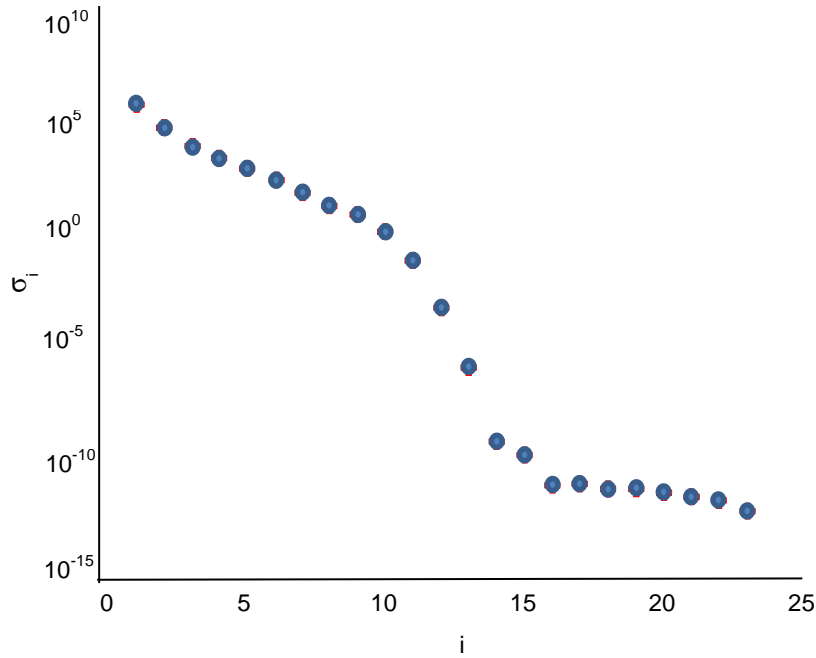


Figure 2.8 – Singular values of \mathbf{A}_{OP} matrix from one-dimensional axisymmetric problem

Åkesson et. al. (2008) used a form of a Tikhonov regularization scheme (discussed later in Section 2.5.2.2.2) to address the ill-posed nature of the system. Since the system used in the study was full-rank, the researchers were able to show how various parameter selection techniques could be used to determine the optimal regularization parameter used for the Tikhonov regularization scheme.

While the axis-symmetric assumption circumvents the rank-deficient and reduces ill-posed nature of the reconstruction problem, more generally this assumption is invalid and therefore non-symmetric

methods must be used. The following section will discuss two-dimensional tomographic algorithms of both frequency and algebraic formulations as well as each of the algorithms' applicability.

2.5.2 Two-Dimensional Tomographic Reconstructions

While employing a one-dimensional reconstruction domain can greatly reduce the complexity of the tomographic reconstruction, in many applications the axisymmetric assumption is invalid, requiring the use of two-dimensionally varying reconstruction fields. The following section will discuss frequency and algebraic based reconstruction methods for solving the 2D tomography reconstruction.

2.5.2.1 Frequency-Based Reconstruction Algorithms

Frequency-based tomographic reconstruction algorithms are derived from the “projection-slice” or “Fourier slice” theorem for Fourier transforms (FT) of a two-dimensional function. The projection-slice theorem states that the one-dimensional Fourier transform of a single projection, i.e. $b_i(s_i, \theta_i)$, is equivalent to a slice of the two-dimensional Fourier transform of the object function at an equivalent angle in the frequency domain (Bertero 1998)

$$b(\omega, \theta) = \int_{-\infty}^{\infty} b(s, \theta) e^{-i\omega s} ds \quad (2.12)$$

Given enough projections, the flow field species distribution can be reconstructed from the assembled frequency domain representation by performing a 2D inverse Fourier transform

$$\mathbf{x}(x, y) = \frac{1}{4\pi^2} \int_0^\pi d\theta \int_{-\infty}^{\infty} b(\omega, \theta) |\omega| e^{i\omega(x\cos\theta + y\sin\theta)} d\omega \quad (2.13)$$

which employs the radon transform

$$\mathbf{x}(s, \theta) = \int_{-\infty}^{\infty} \int_{-\infty}^{\infty} \mathbf{x}(x, y) \delta(x\cos\theta + y\sin\theta - s) dx dy \quad (2.14)$$

Though performing the inverse Fourier transform (IFT) requires the continuous frequency spectrum of projection data, the attenuation measurements are taken at discrete uniformly sampled angles of the

physical domain. From the discretely sampled data, the inverse Fourier transform can be computed by interpolating for unknown regions of the frequency spectrum (Williams 1995).

Alternatively, filtered back-projection (FBP) algorithms avoid direct inversion of the frequency spectrum and requirement for a continuous frequency domain. In FBP, each individual angular projection is converted to the frequency domain using the FT, filtered using a high-frequency filter, converted back into the physical domain using the IFT and then back-projected onto the species concentration domain (Williams 1995). The assembly of projections reconstructs the species distribution and the image quality is highly influenced by the number of projections used. Because of the large availability of angular sampling, FBP is widely used as the reconstruction method for commercial CT scanners as many measurements can be taken at different instances (Burdinger 1979, Liu 2012, Peng 1987).

There are three main limitations for the use of frequency-based algorithms in reconstruction algorithms. The first limitation is that without a high number of projections, regardless of the number of beams per projection, large artifacts arise in reconstructed images. Second, the *a priori* information of solution smoothness is implicitly applied to the solution via the interpolation and filtering stages. This implicit application of the priors offers little tunability and modification to the algorithms. The largest drawback of the frequency-based algorithms is the limited detection array geometries that can be utilized for reconstructions. In their unmodified form, Fourier transform algorithms require equally-spaced parallel beam spacing and equally distributed projection angles (regularized arrangements), though methods have been developed to employ fan-beam arrangements as well (Beiting 1992, Peng 1987, Verhoeven 1993, Zhao 1995). The requirement for either fan-beam or regular arrangements severely limits the applicability of the algorithms since some problem geometries offer severely limited space of detection and emission equipment, requiring irregular beam geometries.

The two-dimensional Fourier transform reconstruction method was first used in a lab-scale tomographic chemical species experiment conducted by Santoro et al. (1981). Using a single 3.39 μm He-Ne laser source and pyroelectric detector pair Santoro et al. were able to achieve line-of-sight measurements at three different axial locations downstream of a turbulent methane-air jet in air by

rotating a traversing the optical setup through the jet. The study used a parallel beam geometry with 12 separate projection angles to image the non-symmetrical methane jet. Since all the absorption measurements were taken at separate instances the planar reconstructions produced were time-averaged profiles and were found to agree with results of previous studies.

Wolfe et al. (1982) were the first to extend the Fourier reconstruction method to large-scale problems in 1982 as a remote sensing technology for air pollution monitoring. The study showed how absorption tomography could be applied to domains with optical distances of approximately a kilometer in area using a two-projection fan-beam detection array for a total on 90 simultaneous absorption measurements. Wolfe et al. used the method for cloud imaging and demonstrated that the proposed methods could achieve a tenfold increase in spatial resolution compared to other methods available at the time. The study also showed the methods could increase the distance between remote sensing stations but at a cost of increased experimental complexity.

Beiting (1992) used the two-dimensional Fourier method to reconstruct a similar gas plume as Santoro et al. using a three-projection fan-beam detection geometry for a total of 96 absorption measurements. The main innovation of the work was the ability to simultaneously measure all channels at 200 ns sample rates, which enabled instantaneous phenomena and concentration profiles.

2.5.2.2 Algebraic Reconstruction Algorithms

The alternative to frequency-based reconstructions algorithms are algebraic reconstruction techniques (ARTs). ARTs use the geometric location of each individual detection beam relative to a discretized flow field domain as outlined in Section 2.3, to form the rank-deficient matrix system outlined in Equation (2.4). There are two major advantages of ARTs with respect to frequency-based reconstructions. The first benefit of an ART algorithm is the flexibility in detection array geometries. Unlike methods based on the Fourier transform there are no limitations of the structure of the detection array. This fact means that ART algorithms can be applied to problems in which areas of the flow field or surrounding environment do not permit a regular, dense angular and axial spacing between beams.

Examples of limited geometries include the imaging hydrocarbons within a cylinder of an automotive engine (Wright 2005, 2010). In this example a range of angles along the outside of the flow field are unsuitable for detection equipment (laser/detector) due to the neighbouring cylinder. The second benefit of ART reconstruction algorithms is the mathematical flexibility for implementation *a priori* knowledge on the solution method. The following section will illustrate different ART reconstruction algorithms from previous work and relevant literature.

2.5.2.2.1 Landweber Iterative Methods

The Landweber iterative method is an algorithm original developed by Landweber in 1950 for solving discrete ill-posed problems arising from Fredholm integral equations of the first kind (Landweber 1951). Assuming an ill-posed linear inverse problem $\mathbf{Ax} = \mathbf{b}$, where the solution \mathbf{x} is unknown, the Landweber method attempts to minimize the residual norm squared,

$$G(\mathbf{x}) = \frac{1}{2} \|\mathbf{b} - \mathbf{Ax}\|_2^2 \quad (2.15)$$

The general form of the algorithm is defined by the update model

$$\mathbf{x}^{k+1} = f\left[\mathbf{x}^k + \alpha \mathbf{A}^T (\mathbf{b} - \mathbf{Ax}^k)\right] \quad (2.16)$$

where α is a positive non-zero relaxation parameter, k is the iteration step number and f is a regularization operator for incorporating *a priori* knowledge (Hansen 2002). The value of α is chosen heuristically, though in most cases an upper limit for iterative stability can be computed from Yang et al. (1999) expression

$$0 < \alpha < 2\left(\|\mathbf{A}^T \mathbf{A}\|_2\right)^{-1} \quad (2.17)$$

The algorithm can either be initiated from a null estimate of the solution, i.e. $\mathbf{x}^0 = 0$, or can be approximated from the forward solution, $\mathbf{x}^0 = \mathbf{A}^T \mathbf{b}$, using \mathbf{A}^T as an approximation of the kernel inverse. The method repeatedly compares the measurements to those that would be formed from the previous iteration's estimate for the solution using the forward operator \mathbf{Ax}^k and the discrepancy is mapped back

onto the solution using the kernel. The classical form of the Landweber method, without the regularization operator f , is well suited for the reconstruction of discrete ill-posed problems in which small singular values of the \mathbf{A} matrix result in amplification of error in the recovered solution. The method progressively suppresses the effects of small singular values of the system with each iteration, k (Bertero 1998, Hansen 2002). In the limited data tomographic problem, the system is also rank-deficient, meaning only pixels subtended by a laser are updated at each iteration. To address the rank-deficiency of the system, the regularization parameter, f , imposes constraints and incorporates *a priori* information about the solution after every iteration so that a unique solution can be determined.

The Landweber method has been implemented and favoured by the Industrial Process Tomography (IPT) group at the University of Manchester (Garcia-Stewart 2003, Pal 2008, Terzija 2011). The group has also investigated several different regularization methods for addressing the rank-deficient and ill-posed nature of the solution, i.e. the functionality of f in Equation (2.16). The first regularization method investigated by the group was the use of non-negativity and two-dimensional mean window filtering at each successive Landweber iteration (Garcia-Stewart 2003). Non-negativity is imposed by searching the candidate solution after each iteration and forcing all negatively-valued pixels to zero. Mean window filtering involves updating a pixel of the candidate solution with the mean value of pixel values from a group of neighbouring pixels (subtended by a square window centered at the pixel of interest). This process is repeated for each pixel of the candidate solution in an effort to impose the *a priori* knowledge of concentration distribution profile smoothness on the solution. Further improvement to the reconstructed images was accomplished by regularizing the candidate solutions by passing a two-dimensional low-pass band filter on the solution, which limits the high-frequency spatial components of the candidate solutions. The stopping criteria used for this implementation of the reconstruction algorithm used a convergence functional,

$$\Delta I = \frac{\sum_n |\mathbf{x}^{k+1} - \mathbf{x}^k|}{\left| \sum_n \mathbf{x}^{k+1} \right|} \quad (2.18)$$

and a convergence tolerance of $\Delta I < 0.01$ for algorithm termination. The resulting reconstructed images from the mean window filtering method resulted in smearing due to the large window sizes used relative to the scale of flow artifacts (i.e. vortices). The degree of smearing can be modified by the choice of window size but otherwise the proposed algorithm had little versatility in specifying the importance of the measurement data relative to that of the *a priori* information (i.e. smoothness).

Further work by the IPT group led to the use of median, rather than mean, filtering to impose smoothness on the reconstructed solution (Wright 2010). Using the median value of the window filter was found to reduce the solution's sensitivity to extreme pixel values which caused large-valued pixel values to propagate through the iterative solution. Consequently, median filtering was better able to remove erroneous values in the solution without reducing sharpness in the reconstruction in addition to reduced error values from simulated experiments (Wright 2010).

Most recently, the IPT group has presented the application of wavelet filters in the spatial domain (rather than the frequency domain) for modified Landweber reconstructions (Terzija 2011). In their work, a two-dimensional discrete wavelet transform (DWT) is used to perform the function of a smoothing filter on the solution. The method begins by decomposing a candidate solution 2D image, \mathbf{x}^k , into three levels of discrete wavelet transform. Each decomposed level contains a detail subband, which contains information about sharp edges that arise from beam path artifacts, and an approximation subband which represents the subject distribution. In an effort to remove the sharp edge artifacts, a smoothed solution is reconstructed by applying the inverse DWT to only the approximation sub-bands. Additionally, filtering is applied to the approximation sub-band prior to inversion by thresholding the coefficients in an effort to further remove solution discontinuities. The use of wavelet filters was found to greatly improve reconstructed images from simulated absorption data as the solutions showed significant qualitative and quantitative improvement to that of mean and median window filtering (Terzija 2011). DWT regularization was able to localize the approximate species distribution after the first iteration, which greatly reduced algorithm iteration time.

The disadvantage of DWT filtering is the lack of parameter selection techniques for the algorithm. The choice of wavelet transform *mother filter*, level of decomposition and level of coefficient thresholding must be selected using heuristic techniques. The selection of the parameters can have a very significant impact on the results of the reconstruction and thus without prior study, choosing the optimal parameters can be time consuming and inexact.

IPT researchers at the University of Manchester demonstrated the Landweber reconstruction technique in the first application of laser absorption tomography on a transient phantom at high sample rates (Wright 2005, 2010). The group used a 32-beam regular array and a 27-beam irregular beam array on a 3200 pixel domain to measure the time-resolved species distribution of fuel in a single cylinder of a commercial automotive 4 cylinder 2.0 L engine, directly below the cylinder injection nozzles. To account for attenuation mechanisms not specific to the hydrocarbon (HC) absorption, the group used the dual wavelength ratiometric (DWR) technique which uses two wavelengths, one highly absorbed by (HC) and one with minimal absorption, 1700 nm and 1651 nm respectively, that allowed quantification of droplet scattering effects (Wright 2010). The researchers used a DFB laser source and InGaAs photodiode receivers to successfully image and measure the hydrocarbon species distributions at effective frame rates of 3000-4000 fps dependent upon the operating speed of the engine.

2.5.2.2.2 Tikhonov Regularization Methods

The Tikhonov regularization method is a direct regularization technique originally intended for the treatment of discrete ill-posed problems. The method was discovered independently by Tikhonov and Phillips in 1962 to incorporate additional *a priori* information regarding the desired solution through the addition of an additional n equations to the problem formulation in Equation (2.4). The two most common implementations of Tikhonov regularization impose assumptions about either the size of degree of smoothness of the solution. The general form of Tikhonov regularization in discrete ill-posed problems leads to the minimization of the functional (Bertero 1998, Hansen 2002, Piccolomini 1999)

$$\mathbf{x}^* = \arg \min \left\{ \|\mathbf{Ax} - \mathbf{b}\|_2^2 + \lambda^2 \|\mathbf{Lx}\|_2^2 \right\} \quad (2.19)$$

where λ is the regularization parameter that controls the influence of the prior information on the recovered solution. The function of the regularization term depends on the choice of the $n \times n$ regularization matrix \mathbf{L} for which the norm $\|\mathbf{Lx}\|_2^2$ is minimized.

In discrete ill-posed problems, Tikhonov regularization is used to reduce the ill-posedness of the system by augmenting the small singular values of the \mathbf{A} matrix responsible for noise amplification. In many applications Tikhonov regularization with a smoothing matrix is used to stabilize a reconstruction to small perturbations in the measurement data that can lead to large perturbations in the recovered solution (Hansen 1990, 2002).

The overall function of Tikhonov regularization is also heavily dependent on the value of regularization parameter, λ , which scales the influence of prior information. In the case of full-rank discrete ill-posed linear problems there are three parameters selection techniques to aid in the chosen value of λ . These methods include L-curve curvature, generalized cross-validation and discrepancy principal techniques. For a full description and derivation of these techniques the reader is directed to the work of P.C. Hansen (1990, 1992, 2002).

The first application of Tikhonov regularization to laser absorption tomography was presented by Cai et al. (2008) who used 2D Tikhonov smoothing for both species and temperature distribution reconstructions. In their work, a 2D smoothing matrix was chosen and defined by

$$L_{ij} = \begin{cases} 1 & \text{if } i = j \\ -1/k & \text{if } j \text{ neighbours } i \\ 0 & \text{otherwise} \end{cases} \quad (2.20)$$

where for an k is the number of neighbouring pixels. In Cai et al.'s work, $k=8$ for an interior pixel, effectively using the surrounding eight pixels to approximate the discrete gradient operator (Cai 2008, Ma 2008, 2009, 2013). With a suitable amount of *a priori* knowledge about the temperature distribution coupled with the high number of measurements used in the study, 20 beams with 10 wavelengths per

projection, and relatively low number of unknowns, 10×10 discretized domain, the authors were able to use L-curve curvature as a parameters selection technique. The authors then created a simulated annealing algorithm to minimize the functional Equation (2.19) (Cai 2008).

In 2013, members of Cai's group, Ma et al. (2013) applied the technique by reconstructing the two-dimensional water-vapour species distribution at the exhaust of General Electric J85 aero-propulsion engine using a 30-beam, 2-projection rectilinear detection geometry and a 15×15 reconstruction domain at unprecedented temporal response speeds of up to 50 kHz. Tunable diode lasers allowed the group to be the first to employ hyperspectral tomography on a large-scale problem.

Daun (2010) was the first to apply Tikhonov regularization to limited-data tomography problems and also provided a robust parameters selection technique for such applications. The regularization matrix used by Daun (2010) used the same formulation as Equation (2.20) with the exception that only the surrounding four neighbors (i.e. $k=4$) of an interior pixel are used in the smoothing matrix \mathbf{L} . The use of only the four of the neighbouring cells, rather than eight, is more numerically and physically accurate than the form used by Cai et al. A Taylor series expansion of the differential operator does not include values neighbouring the point of interest on the diagonals (i.e. NE, NW, SE, SW) whereas Daun's definition of \mathbf{L} can be directly derived from a Taylor series expansion leading to a central finite difference formulation.

In Tikhonov formulations of rank-deficient problems, adding $\lambda \mathbf{L} \mathbf{x} = 0$ fills in the null singular values thereby "spanning" the nullspace of \mathbf{A} , resulting in a constrained least squares minimization problem (Daun 2010)

$$\mathbf{x}^* = \arg \min \left\{ \left\| \begin{bmatrix} \mathbf{A} \\ \lambda \mathbf{L} \end{bmatrix} \mathbf{x} - \begin{bmatrix} \mathbf{b} \\ 0 \end{bmatrix} \right\|_2^2 \right\} \text{ s.t. } \mathbf{x} \geq 0 \quad (2.21)$$

In rank-deficient problems, traditional parameter selection techniques, such as L-curve and cross-validation, cannot be utilized because they are based on the premise that the correct solution corresponds to the smallest solution norm $\|\mathbf{x}\|$, which is not true here due to the nontrivial null space component, \mathbf{x}^n (Hansen 1992, Zdunek 2007). Daun (2010) instead showed that the singular values of the augmented

kernel matrix in Equation (2.21) provide guidance for choosing λ . Daun (2010) found that the singular values of the augmented matrix should not overwhelm the original m nontrivial singular values of \mathbf{A} that correspond to laser attenuation measurements to avoid reconstruction error resulting from oversmoothing and undersmoothing of the tomography domain.

The following section will discuss the formulation of a novel reconstruction algorithm incorporating concepts of the level set method into the solution process. The mathematical basis of the algorithm arises via the consideration of a new solution prior yet to be considered in reconstruction algorithms.

3. LEVEL SET METHODS AND RECONSTRUCTION ALGORITHMS

In the study of gaseous and chemical species tomography, the most commonly used priors for distribution reconstruction are species non-negativity and spatial profile contiguity, as previously discussed in Section 2.5. Further improvements to reconstruction accuracy of tomographic algorithms require additional and more specific prior knowledge about the expected solution. This chapter will discuss the design of a novel tomographic reconstruction algorithm for chemical species flows which imposes more sophisticated *a priori* information through the level set method (LSM), an interface tracking technique, which to this point has not yet been incorporated into chemical species tomographic reconstruction algorithms.

The performance of the LSM reconstruction algorithm is assessed by performing a simulated laser absorption tomography experiment using a computational fluid dynamics (CFD) derived mixed buoyant turbulent methane plume. Qualitative and quantitative comparison between Tikhonov and LSM reconstructions is discussed along with computational costs of each algorithm.

3.1 Tomography Priors for Turbulent Plumes and Jets

Without addition of physically valid priors to the experimental data, the rank-nullity theorem states that a unique stable solution cannot be recovered. When solving rank-deficient problems, where the measurement data is insufficient to specify a unique solution, like that of limited data absorption tomography, the original problem formulation must be augmented with the incorporation of additional *a priori* information. The accuracy of a reconstruction arising from such problems is then directly related to the applicability and validity of the *a priori* information.

The commonly used non-negativity prior is very intuitive as a negative concentration of species is non-physical; the lowest concentration measure possible is zero. The spatial profile smoothness prior is established based on empirical observation of gaseous flows and fluid dynamics analysis. Empirical studies turbulent jet flows for example, like those in previous laser absorption tomography studies, show a smooth two-dimensional planar variation of temperature, velocity and species concentration particularly

perpendicular to the axial flow direction (Davidson 2002). These smoothly-varying distributions are found both in instantaneous and time-averaged profiles and can be attributed to the strong effects of diffusion (molecular and turbulent) associated with gas flows, particularly turbulent flows (Chu 1999, Gazzah 2010, Pitts 1991). Fick's law quantitatively describes the diffusive flux of species based on the local concentration gradient in the flow, and promotes a smoothly varying local concentration profile (Incopera 2007).

Investigating novel *a priori* information, a common feature can be observed by noting the type of flows studied in past chemical species absorption tomography work. One phenomenon that has been studied extensively has been the nature of turbulent jet in free or co-flow. From empirical and analytical study of turbulent jets and plumes at moderate distances downstream of the jet/plume origin, a clear interface between the jet/plume flow (typically the species of interest) and the free or co-flow fluid has been observed and studied (Chu 1999, Davidson 2002, Gazzah 2010, Pitts 1991). These well-defined interfaces essentially bound regions of the domain in which the species of interest are present arising from upstream advection.

The likelihood of these bounded regions representing a contiguous concentration profile being observed is solely based on the properties of the flow itself. For example, the divergence of a turbulent jet in a duct of free or co-flow is specified by the spread rate, S , shown in Figure 3.1, defined as $S \equiv \delta r_{1/2} / \delta x$ where x is the axial distance from the virtual origin of the jet and $r_{1/2}$ is the jet's half-width defined as $U(x, r_{1/2}) = \frac{1}{2}U(x, 0)$ where $U(x, 0)$ is the axial velocity at the centre-line (Pope 2000). Using geometric relations, for a given duct width, D , there exist some length L before which the jet has not diffused to the duct walls. Using trigonometric relations, this length can be defined as $L \approx D/2S$. Based on observation, at any axial distance downstream of the jet origin less than L we expect to find a well-defined interface between the jet fluid and co-flow fluid. Though this statement is based on a turbulent jet flow, it has applicability to several other problems such as that of the injected fuel into an automotive engine and exhaust of an aircraft engine as in previous CST studies (Wright 2005, 2010).

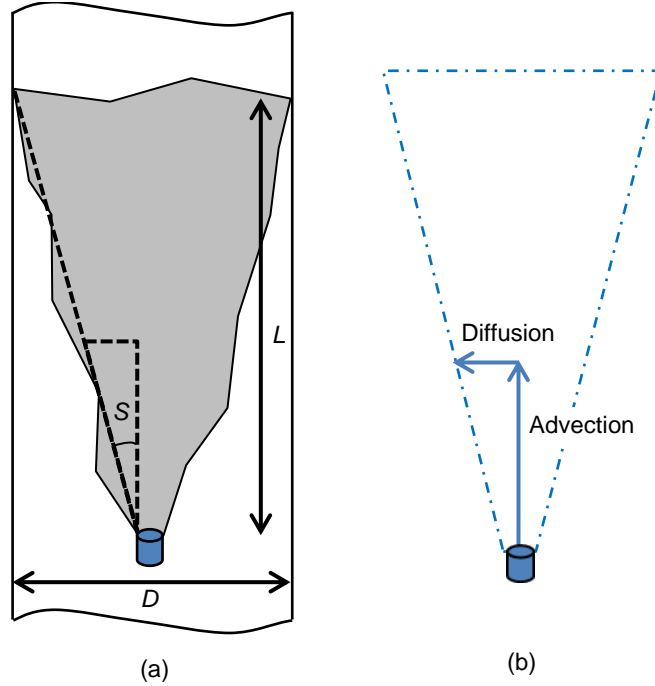


Figure 3.1 – (a) Spreading of a turbulent round jet, (b) Mass transport terms

There are two main contributing factors that dictate the magnitude of the spreading rate S : advection (momentum or buoyancy driven) in the axial direction and diffusion (molecular and turbulent) which can occur in all directions, but most notably perpendicular to the flow. The ratio between these two factors can be used to quantify the jet divergence rate, thus flow with higher ratio of advection-to-diffusion can expect to have larger lengths where an interface is present.

It would seem that reconstructions that promoting a defined species interface and a contiguous flow field for the distribution profile may lead to reduced ill-posedness and increased accuracy. The addition of new *a priori* information creates an additional obstacle as a method to incorporate the additional knowledge into the reconstruction must be investigated. Tikhonov regularization cannot reconstruct a defined interface between the plume and the surrounding co-flow or free-flow and does not promote a contiguous solution; instead, the smoothing action of the $\mathbf{Lx} = 0$ equations to the system diffuses the concentration over the entire solution space.

The following section will discuss the use of the level set method (LSM) to define interfaces between regions where the species of interest are present for use in a tomographic reconstruction

algorithm. This innovation allows the application of smoothing (regularization) in these distinct regions rather than across the entire reconstruction domain, reducing or eliminating the presence of the smearing artifacts observed in Tikhonov and Landweber reconstructions.

3.2 Level Set Method Overview

The level set method was developed by Osher and Sethian as a technique to model and track the dynamic motion of curves, surfaces and interfaces. The advantage of the level set method compared to traditional interface discretization techniques is the parameter-free approach which is particularly good for dynamically changing topological forms (Osher 2003). Since its introduction in 1987, the level set method has found application in a variety of fields including image segmentation and analysis (Ho 2002, Perona 1990), computational physics (Sussman 1994) and computer graphics (Zhao 2001).

In the traditional implementation of the level set method, a two-dimensional boundary between two distinct phases is implicitly represented by the intersection between a three-dimensional surface, $\phi(\mathbf{p}, t)$, defined at every point, $\mathbf{p}=[p_x, p_y]^T$, termed the *level set function* (LSF) and two-dimensional finite plane, typically $\phi=0$, referred to as the *level set*. Using this formulation, the two-dimensional boundary between the two phases, Γ , is defined

$$X = \begin{cases} X_{int}, & \phi > 0 \\ \Gamma, & \phi = 0 \\ X_{ext}, & \phi < 0 \end{cases} \quad (3.1)$$

where X_{int} is the region within the interface boundary and X_{ext} is outside the boundary, as shown in Figure 3.2. The main objective of level set method problems is to evolve the interface, Γ , for a specific purpose. In the context of image segmentation, for example, the algorithm objective is to evolve an initial level set function, ϕ_0 , so that the interface, Γ , segments the original image along sharp gradients and edges, effectively outlining an area of interest from the neglected background. For traditional boundary/shape reconstruction problems, the objective is to recover the phase boundary of the object from a set of measurements.

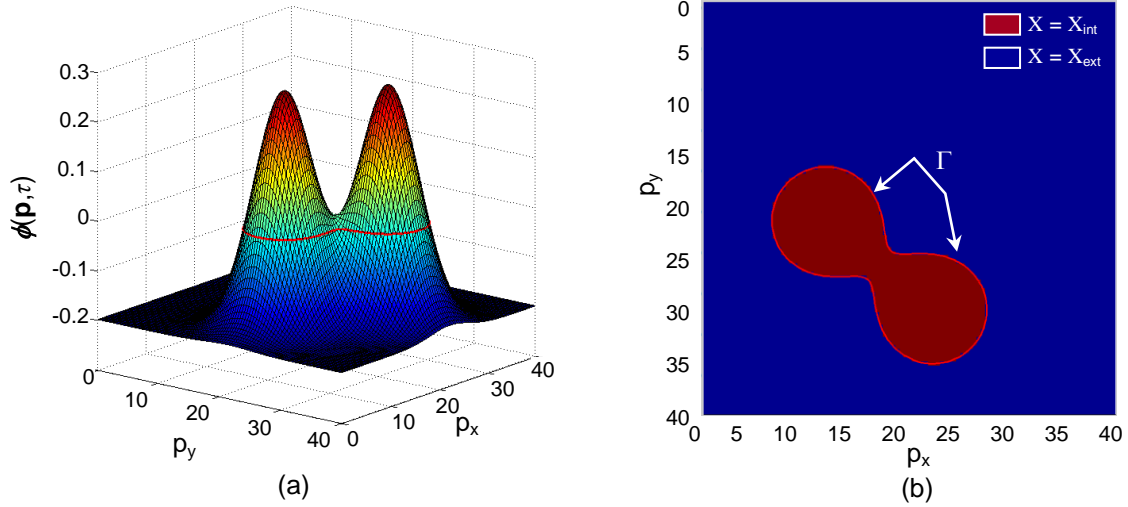


Figure 3.2 – Classical level set geometry (a) sample level set function; (b) corresponding implicit X-domain via Equation (3.1)

The evolution of the level set function, and thus the implicit interface, is described by taking the differentiating the LSF equation $\phi(\mathbf{p}, t)$

$$\frac{\partial \phi}{\partial t} + \nabla \cdot \mathbf{v}(\mathbf{p}, t) = 0 \quad (3.2)$$

producing a Hamilton-Jacobi partial differential equation where \mathbf{v} is the velocity of ϕ at every point, \mathbf{p} , in the X domain and t is iterative time for the evolution. If ϕ is restricted to evolve normal from the surface as some speed, F , then

$$F(\mathbf{p}, t) = \mathbf{v}(\mathbf{p}, t) \cdot \mathbf{n}(\mathbf{p}, t) = \mathbf{v}(\mathbf{p}, t) \cdot \frac{\nabla \phi(\mathbf{p}, t)}{\|\nabla \phi(\mathbf{p}, t)\|} \quad (3.3)$$

By combining Equations (3.2) and (3.3), the level set function changes according to the equation

$$\frac{\partial \phi}{\partial t} + F \|\nabla \phi\| = 0 \quad (3.4)$$

commonly referred to as the *level set equation* (Osher 2003). The time-dependant scalar velocity field $F(\mathbf{p}, t)$ defines the motion of the level set function through numerical integration of Equation (3.4) from some initial condition, ϕ_0 .

Traditionally, the level set function is initialized as a signed distance function (SDF), which satisfies the eikonal equation,

$$\|\nabla \phi\| = 1 \quad (3.5)$$

locally throughout the level set function domain, shown in Figure 3.4 (a). Level set function initialization as a SDF is often chosen for iterative stability of the algorithm as the unity gradient alleviates the effect of small changes near the interface Γ on the implicit X domain (Litman 1998, Osher 2003). In the event very shallow gradients are present in the region of the level set, small changes in the level set function can translate to large changes in the interface location defined by Equation (3.1). As a result, in many LSM applications it is preferable to maintain a SDF through the progress of the level set evolution to avoid numerical and computational divergence as well as promote a contiguous phase region.

During the evolution of a LSF it is common for the function to develop irregularities, i.e. local spikes, as well as deviation from the eikonal condition. To overcome these irregularities, a common remedy is to periodically re-initialize the function as a SDF while maintaining the same location of Γ , which has been shown to maintain stable interface evolution. In this procedure, the irregular LSF is modified using the re-initialization equation

$$\frac{\partial \phi}{\partial t} = \text{sign}(\phi) [1 - \|\nabla \phi\|] \quad (3.6)$$

where $\text{sign}(\cdot)$ is the sign function (e.g. $\text{sign}(-3) = -1$, $\text{sign}(3) = 1$) (Osher 2003). Equation (3.6) is the most commonly used and simplest form of the re-initialization equation but there has been extensive study on the subject for more computationally efficient schemes. The main drawback associated with re-initialization during the algorithm is that in many cases the position of the zero-level set of the function can be incorrectly moved away from its original position, inherently changing the function of the algorithm. For reasons such as these, re-initialization is typically avoided as much as possible since there is no general procedure for the use of the schemes (Li 2010).

3.3 Application of LSM to Linear Inverse Theory

A level set method approach for inverse problems relating to shape, or boundary, reconstruction was presented by Santosa (1996). Santosa showed for a linear inverse problem $\mathbf{A}(\mathbf{u}) = \mathbf{g}$ in which the

unknown vector \mathbf{u} contains only two discrete values, as in Equation (3.1), could be solved using a level set formulation in which the velocity field, F in Equation (3.4), was defined to iteratively minimize the residual

$$K(\mathbf{u}) = \frac{1}{2} \|\mathbf{A}(\mathbf{u}) - \mathbf{g}\|_2^2 \quad (3.7)$$

beginning from some initial LSF. Santosa showed for various inverse problems the residual $K(\mathbf{u})$ is reduced by the velocity field

$$F(\mathbf{p}, t) = -\mathbf{J}(\mathbf{u})^T [\mathbf{A}(\mathbf{u}) - \mathbf{g}] \quad (3.8)$$

where $\mathbf{J}(\mathbf{u})$ is the Jacobian of $\mathbf{A}(\mathbf{u})$ at \mathbf{u} . Therefore, for a full-rank inverse problem, the level set evolution is defined as

$$\frac{\partial \phi}{\partial \tau} = -(\mathbf{J}(\mathbf{u})^T [\mathbf{A}(\mathbf{u}) - \mathbf{g}]) \|\nabla \phi\| \quad (3.9)$$

Santosa notes, however, that the solution algorithm does not address the underlying ill-posedness of the inverse problem, and in the case of the limited data tomography, does not address the rank-deficiency of \mathbf{A} . Santosa's algorithm also requires periodic re-initialization to avoid the effects of shallow gradients and the interface and numerical divergence.

Santosa's work illustrates that choosing the scalar velocity field as the gradient descent of the residual Equation (3.7) is a suitable choice for level set evolution for solving inverse problems. In the context of the linear laser absorption tomography problem $\mathbf{Ax} = \mathbf{b}$, the Jacobian $\mathbf{J}(\mathbf{u})$ is simply the kernel matrix \mathbf{A} where \mathbf{u} in our problem is the species distribution vector \mathbf{x} .

3.4 Level Set Evolution Regularization

Due to the computational cost and modification of the zero level set location, re-initialization is often avoided as much as possible. Yet in some applications, i.e. rank-deficient and ill-posed problems, regularization of the solution, and thus the LSF evolution, is required. Li et al. (2005) pioneered methods for level set evolution regularization and presented a new level set method formulation that allows LSF

deformation that mitigates the use of re-initialization. In their work, Li et al. proposed an energy functional

$$E(\phi) = E_{\text{ext}} + \mu R(\phi) \quad (3.10)$$

to be minimized at every iteration where E_{ext} is a certain parameter to drive the motion of the level set function to a desired goal, $R(\phi)$ is the level set regularization term and $\mu > 0$ is a regularization parameter controlling the influence of prior information. In Li et al.'s work $R(\phi)$ is defined as the deviation of ϕ from a signed distance function and thus minimizing $R(\phi)$ provides a well-conditioned level set function, i.e. one that satisfies the eikonal condition. This work showed that the derivative of Equation (3.10) can describe the level set evolution to iteratively minimize the total energy of the system by evolving ϕ in the steepest descent direction of $E(\phi)$

$$\frac{\partial \phi}{\partial t} = -\frac{\partial E}{\partial \phi} = -\frac{\partial E_{\text{ext}}}{\partial \phi} - \mu \frac{\partial R(\phi)}{\partial \phi} \quad (3.11)$$

The regularization term is defined as

$$R(\phi) = \frac{1}{2} \int_X s(\|\nabla \phi\|) d\mathbf{p} \quad (3.12)$$

where $s(\cdot)$ is a heuristic potential function of the gradient of ϕ . Defining $d_s(k) \equiv s'(k)/k$ it can be shown that (Li 2005)

$$\frac{\partial R}{\partial \phi} = -\nabla \cdot [d_s(\|\nabla \phi\|) \nabla \phi] \quad (3.13)$$

To promote a level set function that satisfies the eikonal condition, perhaps the most obvious choice for $s(\|\nabla \phi\|)$ is to set $s = (\|\nabla \phi\| - 1)^2$, which penalizes deviation of ϕ from an SDF by comparing the magnitude of the gradients to unity at every point in the domain. Minimizing this form of $R(\phi)$ enforces the eikonal condition over the entire domain $\mathbf{p} \in X$, but the approach can result in undesirable oscillations near the level set Γ . Li et al. later presented the distance regularized level set evolution (DRLSE) that allows flat regions in ϕ (Li 2010). The method incorporates an improved potential that promotes

$\|\nabla\phi\| = 1$ if the magnitude of the gradient is greater than 0.5, and $\|\nabla\phi\| = 0$ otherwise. In this work, the potential function was defined as

$$s(t) = \begin{cases} \frac{1}{(2\pi)^2} [1 - \cos(2\pi t)], & \text{if } t \leq 1 \\ \frac{1}{2}(t-1)^2, & \text{if } t \geq 1 \end{cases} \quad (3.14)$$

In addition to promoting a regular phase interface, the stability introduced by $R(\phi)$ in Eqs. (3.13) and (3.14) permits significantly larger time steps, which decreases the algorithm run-time, and also allows integration by explicit Euler finite-differencing instead of more complex schemes (Li 2010). The regularization scheme presented in Li et al.'s work also allows the use of general initialization of the level set, such as step functions, which further decrease the computational workload of the algorithm.

In Li et al.'s work the values of μ are bounded by the Courant-Freidrichs-Lewy (CFL) condition of iterative numerical stability, which in the context of a three-dimensional implicit level set function states that $\mu \cdot \Delta t < 0.25$ (Gilboa 2002, Li 2010). Li et al. (2010) also showed that the regularization method was fairly insensitive to μ , providing the CFL condition is satisfied.

3.5 Extension to laser absorption chemical species tomography

All level set algorithms for tomographic reconstructions to date have focused on binary-valued domains in which a discretized pixel can either possess one of two values, effectively creating an object boundary reconstruction problem (Litman 1998). In chemical species tomography problems, however, the unknown species concentration distribution is a real-valued continuous domain within the bounded regions of Γ . To accommodate a continuous distribution for representation of the gas species distribution in the X-domain, the LSF can be mapped to the species distribution domain by modifying Equation (3.1)

$$\mathbf{x} = \begin{cases} \phi, & \phi > 0 \\ \Gamma, & \phi = 0 \\ 0, & \phi < 0 \end{cases} \quad (3.15)$$

as shown in Figure 3.3.

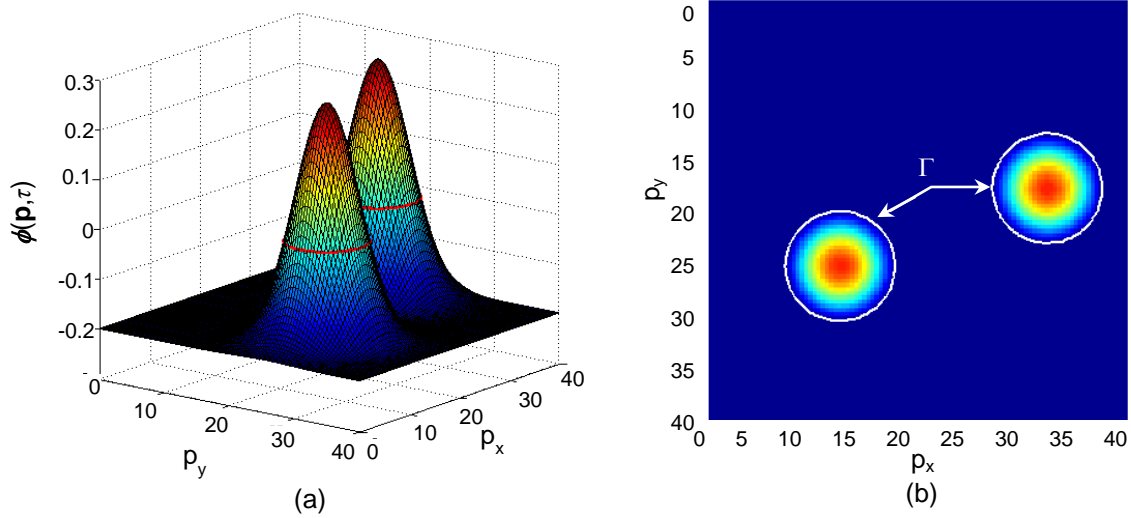


Figure 3.3 – Continuous domain level set geometry (a) sample level set function; (b) corresponding implicit X-domain via Equation (3.15)

This new implicit domain specification allows the concentration distribution to possess any non-zero value which is defined by the magnitude of the discretized level set function above the specified level set, as shown in Figure 3.3. An alternate form of Equation (3.15) is $x_j = \phi_j H(\phi_j)$ where x_j is the gas concentration distribution in cell j centered at $\mathbf{p}_j = [\mathbf{p}_{jx}, \mathbf{p}_{jy}]^T$, ϕ_j is the level set function value at \mathbf{p}_j , and $H(\cdot)$ is the Heaviside delta function.

Though the original formulation of a velocity function, F , for solving inverse problems in the work of Santosa was for binary-valued X-domains, the derivation is consistent for problems in which the reconstruction in question is continuously-valued. Modifying Equation (3.8) for the inverse problem formulation Equation (2.4) results in the external velocity force function

$$F = -\mathbf{A}^T [\mathbf{Ax} - \mathbf{b}] \quad (3.16)$$

to be used in a novel gas distribution reconstruction algorithm. Use of the above velocity function defines the partial differential equation

$$\frac{\partial \phi}{\partial t} = \mathbf{A}^T [\mathbf{Ax} - \mathbf{b}] \|\nabla \phi\| \quad (3.17)$$

for level set function evolution to reconstruct the species distribution. However, due to the rank-deficient nature of the tomography problem, Equation (3.17) quickly produces a highly irregular topology of ϕ after only a few iterative time steps. Initializing from a SDF and using an explicit finite difference scheme of Equation (3.17) only updates the pixels subtended by the laser paths, creating a non-physical solution, shown in Figure 3.4 below.

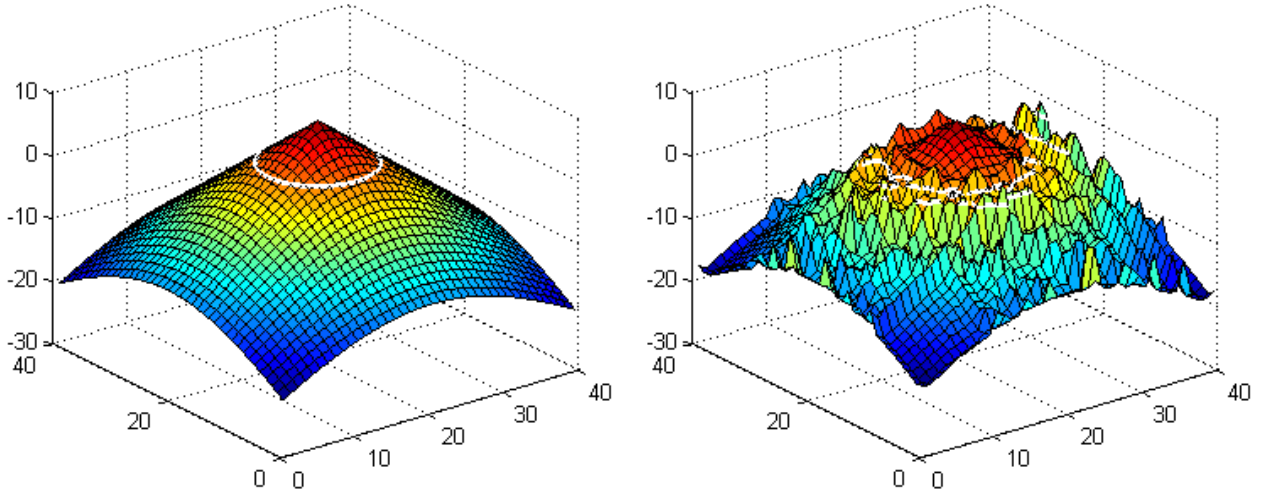


Figure 3.4 – (a) Initialization of ϕ as SDF; (b) Irregular level set function after non-regularized evolution with level set, Γ , shown in white

This exemplifies the need for regularization of the level set evolution to allow the reconstruction of a physically consistent solution. To avoid the formation of irregularities in ϕ and the use of re-initialization the solution can be regularized using Li et al.’s algorithm described in Section 3.4.

Though promoting the eikonal equation as in Li et al.’s work stabilizes the evolving shape of ϕ and discourages the formation of small “pockets” in the vicinity of Γ to produce a contiguous profile, enforcing this condition for level set function values greater than zero (i.e. the gas concentration distribution, \mathbf{x}) is a nonphysical prior. Instead, the smoothness prior can be used as regularization scheme in the region representing the X-domain. To penalize non-smoothness during level set evolution the regularization term for pixels above the level set is defined as the discrete Laplacian,

$$\frac{\partial R}{\partial \phi} = -[\nabla \cdot \nabla \phi] \quad (3.18)$$

which discourages sharp gradients in the LSF surface. Below and at the level set location, i.e. $\phi \leq 0$, the use of the SDF regularization of Li et al. is used to promote a stable evolution of the interface Γ and enforce well-defined boundaries for regions of the gaseous species.

Combining the two deformation terms results in the evolution equation

$$\frac{\partial \phi}{\partial t} = [\mathbf{A}^T (\mathbf{Ax} - \mathbf{b}) \|\nabla \phi\|] + \mu_1 \left\{ \nabla \cdot [d_s(\|\nabla \phi\|) \nabla \phi] \right\} \quad (3.19)$$

at and below Γ , and

$$\frac{\partial \phi}{\partial t} = [\mathbf{A}^T (\mathbf{Ax} - \mathbf{b}) \|\nabla \phi\|] + \mu_2 \{ \nabla \cdot \nabla \phi \} \quad (3.20)$$

for regions above the level set. Integration of these equations using an explicit Euler finite difference scheme results in

$$\begin{aligned} \phi^{k+1} &= \phi^k + \Delta t \cdot \left([\mathbf{A}^T (\mathbf{Ax} - \mathbf{b}) \|\nabla \phi^k\|] + \mu_1 \left\{ \nabla \cdot [d_s(\|\nabla \phi^k\|) \nabla \phi^k] \right\} \right), & \phi^k \leq 0 \\ \phi^{k+1} &= \phi^k + \Delta t \cdot \left([\mathbf{A}^T (\mathbf{Ax} - \mathbf{b}) \|\nabla \phi^k\|] + \mu_2 \{ \nabla \cdot \nabla \phi^k \} \right), & \phi^k > 0 \end{aligned} \quad (3.21)$$

where Δt is the time step. In the regions where $\phi^k > 0$, the trade-off between absorption data and the smoothness criteria is controlled by a regularization parameter, μ_2 , which is analogous to λ in Equation (2.19) of Tikhonov method reconstructions and is not bound by the CFL condition mentioned earlier for Li et al.'s regularization term, μ_1 . The algorithm proceeds until one of two stopping criteria, $K(\mathbf{x}^k) = \|\mathbf{Ax}^k - \mathbf{b}\| < \varepsilon$ or $|K^{k+1} - K^k| < \delta$, is satisfied, where ε and δ are prescribed tolerances.

The proposed level set method reconstruction algorithm described in Equation (3.21) incorporates the traditional chemical species *a priori* information of non-negativity, inherit in the level set formulation, and solution contiguity, applied via the regularization term Equation (3.18), as well as the novel solution prior of the well-defined species boundaries which is incorporating using the regularization scheme of Li et al. The regularization terms, $R(\phi)$, from Equations (3.13) and (3.18) are more implicit form of regularization compared to the Tikhonov smoothing prior. Also, since the Tikhonov method only

approximates the Laplacian operator in \mathbf{L} , the proposed method is more a mathematically accurate for enforcing solution smoothness.

3.6 Results and Discussion

To demonstrate the proposed algorithm a simulated absorption tomography experiment was carried out on a large eddy simulation (LES) of a turbulent buoyant plume as the species of interest. This simulated experiment allows assessment of the level set algorithm in a noise-free data environment, and since the exact solution is known, reconstruction error associated of the algorithm can be found. Conducting the same simulated experiment using the state-of-the-art Tikhonov algorithm described in Section 2.5.2.2 allows comparison of the two methods and permits quantification of the benefits of the novel prior used in LSM reconstructions.

For the LES phantom, the computational domain is a rectangular $1.5 \text{ m} \times 1.5 \text{ m} \times 6 \text{ m}$ enclosure, shown in Figure 3.5 below, filled with air at 298 K and atmospheric pressure. Methane is injected through a $0.2 \text{ m} \times 0.2 \text{ m}$ vent centered at the bottom of the enclosure at 2 m/s, corresponding to a jet Reynolds number of 3000 based on the hydraulic diameter of the duct. The resulting turbulent plume has a densimetric Froude number of 2.2, indicating that the buoyant and momentum forces within the plume are comparable. Further simulation details of the LES parameters can be found in Daun et al. (2011).

The simulated laser attenuation was collected at a height of 3 m above the base on the enclosure, and the tomography domain was defined as a $1 \text{ m} \times 1 \text{ m}$ square, centered in the duct with the laser arrangement shown in Figure 2.6 (b). The beam arrangement was chosen because it is a commonly used 4-projection rectilinear array found in several previous CST experiments (Ibrahim 1999, Rahim 2005). Simulated laser attenuation data was calculated using high-order numerical integration of Equation (2.1), sampled at the rate of 100 Hz for 15 seconds. The tomographic reconstruction domain was discretized into a square 40×40 pixel grid. To quantify the reconstruction error for each of the reconstruction methods the mean absolute percentage error

$$\varepsilon(\mathbf{x}) = \frac{\|\mathbf{x}^{exact} - \mathbf{x}^{rec}\|}{\|\mathbf{x}^{exact}\|} \quad (3.22)$$

was used where \mathbf{x}^{exact} is the exact solution from the LES data and \mathbf{x}^{rec} is the reconstructed solution.

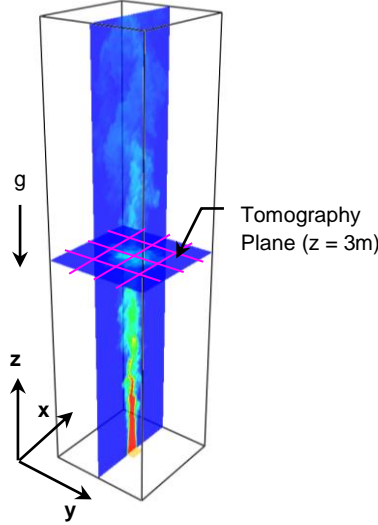


Figure 3.5 – Large eddy simulation of mixed buoyant methane plume

3.6.1 Heuristics

To compare the Tikhonov and LSM reconstruction methods, a variety of parameters must be defined for each technique. In the case of Tikhonov, both the regularization matrix definition and value of the regularization parameter must be selected.

Tikhonov regularization was carried out using the smoothing kernel described by Daun, using the four neighbouring pixels of an interior cell to apply smoothness. As mentioned, Daun showed that λ could be chosen so that the largest m of the n singular values of the augmented matrix do not overwhelm the original m nontrivial singular values of \mathbf{A} . Figure 3.6 shows the singular values obtained from the beam arrangement used and a 1600 pixel domain for various values of λ which suggests that the optimal value of λ is somewhere between 0.01 and 0.1. The regularization parameter value was defined as $\lambda = 0.05$, which previous studies have shown to span the nullspace of \mathbf{A} without overwhelming/filtering the laser absorption data.

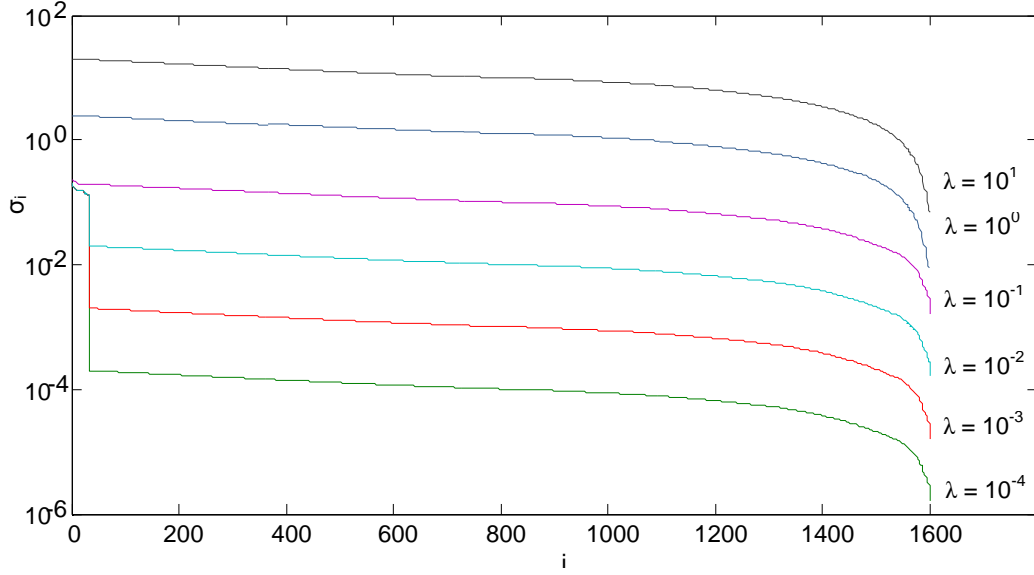


Figure 3.6 – Singular values of A matrix vs. λ for 1600 pixel domain

The algorithm used $\Delta t = 40$, $\mu_1 = 0.05/\Delta t$, as previously recommended by Li et al. for regularization of image segmentation algorithms, which satisfy the CFL condition to iterative stability. The value of the internal LSM regularization parameter, $\mu_2 = 3 \times 10^{-4}$, was selected heuristically. The termination parameters were set equal to values of $\varepsilon = 0.06$ and $\delta = 1 \times 10^{-5}$ for solution convergence.

3.6.2 Results

To demonstrate the effect of level set regularization on the reconstructed solutions, Figure 3.7 shows reconstructions obtained using parameters of $\mu_1 = 0.05/\Delta t$ and $\mu_2 = 3 \times 10^{-4}$ and with ϕ initialized as a SDF. Comparing these results to a non-regularized solution as in Figure 3.4 shows that forcing ϕ to be close to a SDF in the region below the level set and penalizing non-smoothness of ϕ above the level set promotes a spatially-smooth concentration distribution and a smooth Γ that contains a contiguous plume. Without this regularization, on the other hand, the concentration distribution is rougher, and discontinuous regions of methane appear in the tomography plane due to the irregular topology of ϕ .

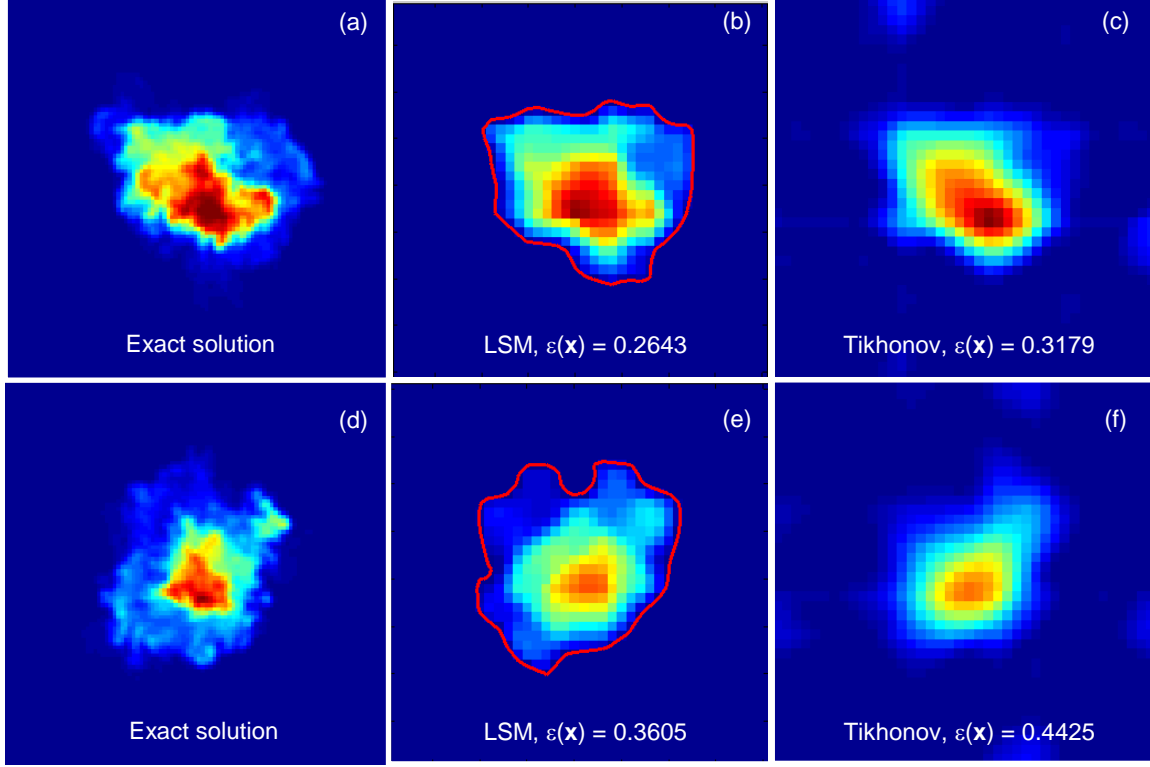


Figure 3.7 – Sample LSM and Tikhonov reconstructions: (a-c) $t = 80s$, (d-f) $t = 100s$, Zero level set, Γ shown in red

Reconstruction errors obtained with the Tikhonov and LSM algorithms are plotted in Figure 3.8, and sample reconstructions for each algorithm are shown in Figure 3.7. The results show the LSM reconstructions are more accurate than those recovered with Tikhonov regularization at all time steps, with average reconstruction errors of $\varepsilon_{\text{LSM}} = 0.3482$ and $\varepsilon_{\text{tik}} = 0.4223$, respectively. The reconstructions in Figure 3.7 qualitatively show that the LSM algorithm better captures integral-scale turbulent features compared to Tikhonov regularization. The LSM reconstructions also show the zero level set, Γ , in red, corresponding to the plume boundary, which agrees well with the general plume shape of the exact solution.

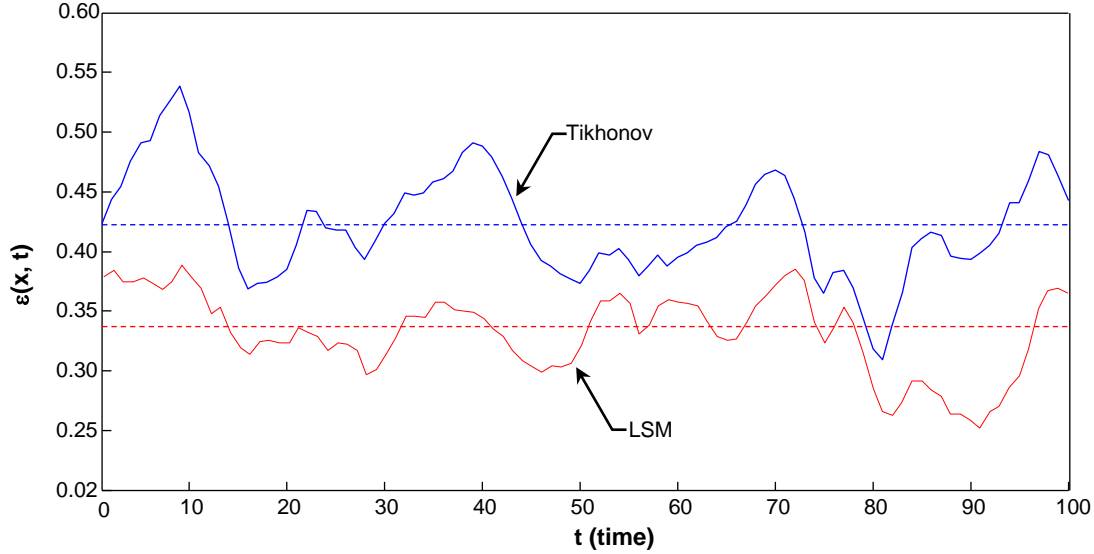


Figure 3.8 – Instantaneous and average reconstruction error results for Tikhonov and LSM algorithms

The superiority of the LSM reconstructions is due to the fact that regularization is introduced implicitly by promoting level set functions that promote a distinct phase interface, a spatially-smooth solution, and also explain the laser absorption data. Consequently regularization is done “locally” over the plume domain, instead of enforcing a smoothing filter over the entire tomography domain, as is done in first-order Tikhonov regularization. Consequently the LSM can: (1) reconstruct locally-changing topologies arising from the sudden appearance and disappearance of turbulent eddies in the tomography cross-section; and (2) predict the discrete boundary between the turbulent plume and the surrounding air. Neither of these attributes applies to Tikhonov regularization, however.

While the LSM provides more accurate reconstructions compared to Tikhonov regularization, it is also far more computationally-expensive; the LSM requires over 1,300 seconds to reconstruct 100 phantoms using a single core of a 2 GHz i7-2630QM Intel processor with 8 GB of installed RAM, while the Tikhonov algorithm needs only 68 seconds.

Another factor that has been shown to have significant impact on the accuracy of chemical species tomography experiments is the arrangement of the laser sources and detectors responsible for the discrete attenuation measurements through the flow field. The following chapter will discuss past

attempts to predict the quality of a beam arrangement in literature and will present a novel fitness function for beam arrangement quality based on resolution matrices. Using the fitness function derived, it is possible to optimize a beam arrangement with imposed constraints. It is also possible to decouple the factors of beam arrangement and number of beams, m , on the expected accuracy of different beam arrangements.

4. ABSORPTION TOMOGRAPHY DETECTION ARRAY OPTIMIZATION

Experimental and numerical studies of laser absorption tomography have shown that the arrangement of laser/detector pairs has a large impact on reconstruction accuracy. Additionally, the high cost and complexity associated with the lasers, detectors and optics demands that the equipment be utilized to its maximum potential. This chapter will discuss a beam arrangement optimization strategy using a Tikhonov framework and resolution matrices. Using the resolution matrix, specified by the locations of the beam transecting the flow field, a fitness function is defined which quantifies the expected reconstruction accuracy associated with the arrangement. The proposed fitness function is validated by investigating how closely it correlates with reconstruction error of simulated limited-data absorption tomography experiments under both noise-free and noisy data conditions.

An objective function is then minimized for a given number of sensors using a genetic algorithm and the unconstrained optimized beam array is shown to outperform other arrangements reported in the literature in terms of reconstruction accuracy. This research also provides a framework for establishing the number of beams needed to achieve a given level of reconstruction accuracy and thus reduce associated experimental costs. Arrangement optimizations are also displayed for various design constraints using an actual chemical species tomography experiment carried out on the exhaust of a gas turbine as a sample problem geometry.

4.1 Beam Arrangement and Reconstruction Accuracy

The location of the optical sensors used to obtain the attenuation measurements is one of the most important factors pertaining to reconstruction accuracy. The strong influence of beam arrangement on the reconstructed solution was demonstrated by Wright et al. during design of the beam arrangement for use in the group's in-engine absorption tomography experiments. Wright et al. showed using simulated absorption data for the beam arrangement in Figure 4.2 (d) that rotating a phantom in the tomography domain 45° resulted in vastly different qualitative and quantitative reconstructions. The deviation of results for the phantom in the different domain locations is shown below in Figure 4.1.

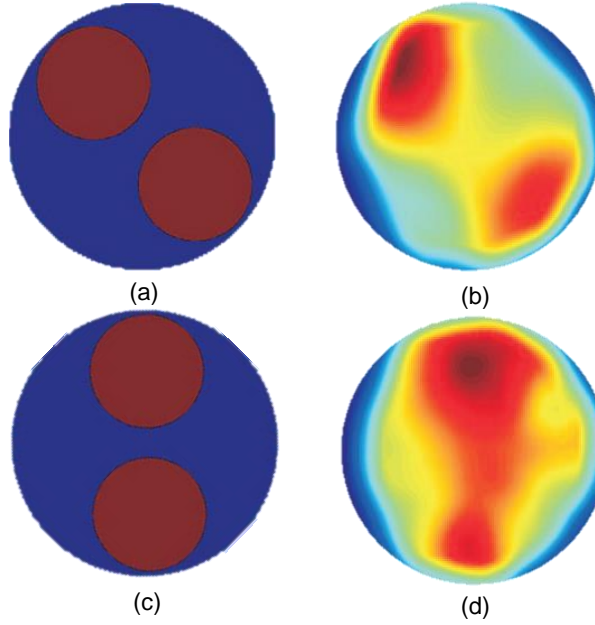


Figure 4.1 – Sample results of simulated experiment using beam arrangement in Figure 4.2 (d), with tiled phantom from (a) shown in (c), corresponding reconstructions (b) and (d) (Figure adopted from Wright et al. 2005)

Daun et al. also showed how the reconstruction accuracy of randomly-sized and located phantom can vary considerably based on the detection arrangement used in the experiment. A selection of beam arrangements investigated in the study is shown in Figure 4.2.

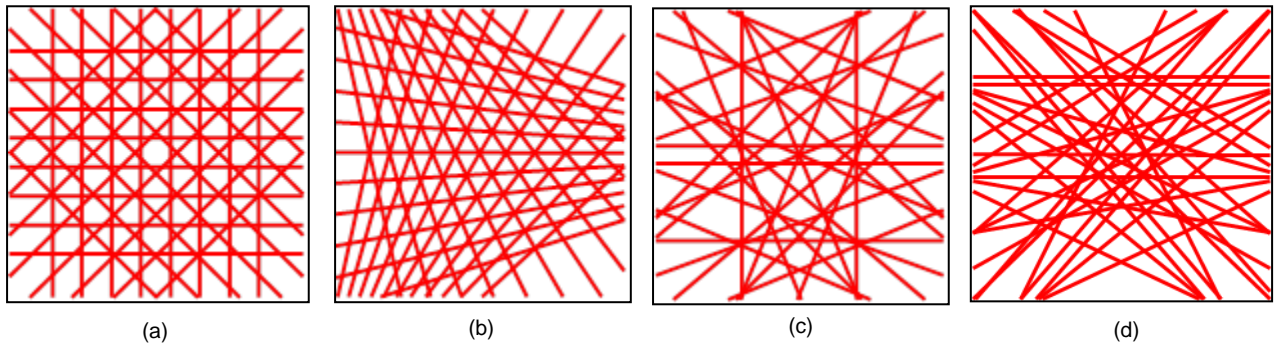


Figure 4.2 – Sample beam arrangements: (a) orthogonal, rectilinear 32 beam, (b) 3-projection fan 33 beam, (c) Irregular 27 beam, (d) Irregular 32 beam

Figure 4.2 (a) illustrates an orthogonal 2-projection rectilinear regular 32-beam arrangement, commonly used tomographic studies because of the simple design and installation of the associated optics (Ibrahim 1999, Rahim 2005). Figure 4.2 (b) shows a 3-projection 33-beam fan arrangement, often found

in industrial settings because of the reduction in light source equipment required (Liu 2012). The arrangements shown in Figure 4.2 (c) and (d) are examples of irregular beam arrangements designed by the IPT group at the University of Manchester for in-engine measurements (Terzija 2008). The irregular nature of arrangements of Figure (c) and (d) arise from the geometric constraints of the neighbouring cylinders which prohibit the placement of launch/receive optics at discrete locations.

Though intuition suggests, and previous studies show, the critical importance of beam arrangements, the only published attempt to develop an optimization strategy for beam locations for absorption tomography was by Terzija et al. (2008). In their work, the authors hypothesized that maximizing the spread of beam locations in radon space, using the $[s, \theta]$ definition of each beam shown in Figure 2.2, improves the reconstruction accuracy of the experiment. The technique is inspired by Fourier-based reconstruction methods and noting that inverting Equation (2.1) by Radon transformation shown in Equation (2.14) involves integrating the attenuation data over $-R \leq s \leq R$, and $0 \leq \theta \leq \pi$ where R is the width of the tomography domain (Bertero 1998). Following this logic, the researchers plotted the coordinates of each beam over radon space as shown in Figure 4.3 for the beam arrangement in Figure 4.2 (c). The researchers argued that maximizing the discrepancy between these points would improve reconstruction accuracy similar to how the accuracy of a numerical integration improves with the discrepancy of the quadrature points.

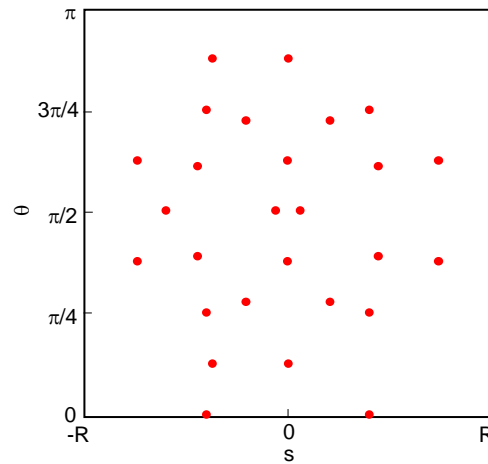


Figure 4.3 – Radon plot for beam arrangement Figure 4.2 (c)

The following section presents the relation between reconstruction error of an actual experiment and the resolution of the system, explained by resolution matrices. By exploiting properties of the resolution matrix created by a candidate arrangement, a optimization strategy is presented utilizing genetic algorithm search methods and incorporating geometric constraints of a given problem domain.

4.2 Resolution Matrices

Resolution matrices are commonly used mathematical tools in discrete geophysical tomography to determine whether model parameters can be independently predicted or resolved, and how regularization limits reconstruction accuracy (Crosson 1976, Curtis 1999, Lees 1989, Menke 1989, Wiggins 1972). For a given linear, full-rank problem defined $\mathbf{G}\mathbf{x}^{\text{true}}=\mathbf{b}^{\text{obs}}$, the reconstructed solution can be estimated using the inversion $\mathbf{x}^{\text{est}}=\mathbf{G}^{\#}\mathbf{b}^{\text{obs}}$ where $\mathbf{G}^{\#}$ is the generalized inverse of matrix \mathbf{G} , and \mathbf{b}^{obs} is the observed measurement data. The resolution matrix for the problem is then derived using simple substitution

$$\begin{aligned}\mathbf{x}^{\text{est}} &= \mathbf{G}^{\#}\mathbf{b}^{\text{obs}} \\ &= \mathbf{G}^{\#}[\mathbf{G}\mathbf{x}^{\text{true}}] \\ &= [\mathbf{G}^{\#}\mathbf{G}]\mathbf{x}^{\text{true}} \\ &= \mathbf{R}\mathbf{x}^{\text{true}}\end{aligned}\tag{4.1}$$

Equation (4.1) displays using a simple derivation how the estimated solution is mathematically related to the true solution via matrix \mathbf{R} , called the *resolution matrix* (Crosson 1976, Curtis 1999, Lees 1989, Menke 1989, Wiggins 1972). In the case that $\mathbf{R} = \mathbf{I}$, each element of \mathbf{x} can be independently and uniquely resolved. If \mathbf{R} is not an identity matrix, the estimated solution is then a weighted average of the true parameters (Wiggins 1972). Fortunately, the resolution matrix of the problem is only the function of the kernel, \mathbf{G} , and is thus independent of the data (Menke 1989).

4.2.1 Resolution Matrices for Limited-Data Tomography

Due to the rank-deficient nature of the matrix equation underlying limited-data tomography problems, the resolution matrix for a given beam arrangement cannot be produced directly from the ART problem formulation, Equation (2.4), since the kernel matrix \mathbf{G} must be at least full-rank to mathematically define the generalized inverse $\mathbf{G}^\#$ (Hansen 2002, Menke 1989). By incorporating the smoothness prior to the problem, however, as shown in Equation (2.21), the problem can be made over-determined and thus the generalized inverse and resolution matrix can be formed. The resolution matrix is derived from the regularized inverse, $\mathbf{A}^\#$, which for the Tikhonov regularization method can be found by (Berryman 1994, Crosson 1976, Hansen 2002, McCarthy 2011)

$$\mathbf{A}^\# = (\mathbf{A}^T \mathbf{A} + \lambda^2 \mathbf{L}^T \mathbf{L})^{-1} \mathbf{A}^T. \quad (4.2)$$

where in our formulation

$$\mathbf{G} = \begin{bmatrix} \mathbf{A} \\ \lambda \mathbf{L} \end{bmatrix} \quad (4.3)$$

The regularized solution can then found via inverse substitution, $\mathbf{x}_\lambda = \mathbf{A}^\# \mathbf{b}$. In real-world implementations the measurement data vector will contain some data noise, i.e. $\mathbf{b} = \mathbf{b}^{\text{exact}} + \delta \mathbf{b}$, where $\delta \mathbf{b}$ is the component of the signal due to measurement noise. The solution is then given by

$$\mathbf{x}_\lambda = \mathbf{A}^\# (\mathbf{b}^{\text{exact}} + \delta \mathbf{b}) = \mathbf{A}^\# \mathbf{b}^{\text{exact}} + \mathbf{A}^\# \delta \mathbf{b} \quad (4.4)$$

By noting the forward problem definition, $\mathbf{A} \mathbf{x} = \mathbf{b}^{\text{exact}}$,

$$\mathbf{x}_\lambda = \mathbf{A}^\# \mathbf{A} \mathbf{x}^{\text{exact}} + \mathbf{A}^\# \delta \mathbf{b} = \mathbf{R} \mathbf{x}^{\text{exact}} + \mathbf{A}^\# \delta \mathbf{b} \quad (4.5)$$

where $\mathbf{R} \in \mathbb{R}^{n \times n}$ is the resolution matrix. Comparing this recovered solution to the exact solution the reconstruction error, $\delta \mathbf{x}$, can be found and separated into two components via

$$\delta \mathbf{x} = \mathbf{x}_\lambda - \mathbf{x}^{\text{exact}} = (\mathbf{R} - \mathbf{I}) \mathbf{x}^{\text{exact}} + \mathbf{A}^\# \delta \mathbf{b} \quad (4.6)$$

where $(\mathbf{R} - \mathbf{I}) \mathbf{x}^{\text{exact}}$ is the *regularization error*, caused by the inconsistency between the measurement data equations, $\mathbf{A} \mathbf{x} = \mathbf{b}$, and the assumed prior information, $\mathbf{L} \mathbf{x} = 0$, while $\mathbf{A}^\# \delta \mathbf{b}$ is the *perturbation error*, due to the amplification of measurement noise in the system (Hansen 2002).

As previously mentioned in Chapter 2, in traditional Tikhonov problems, the system is full-rank yet discrete ill-posed via violation of Hadamard's third criteria, as small perturbations in the data result in large changes in the inverted solution. In these problems, the kernel, \mathbf{A} , is full rank but ill-conditioned, having n nontrivial singular values that range over several orders of magnitude. For these ill-posed problems $\mathbf{Ax} = \mathbf{b}$ completely defines the problem physics and $\mathbf{Lx} = 0$ is added to suppress perturbation error, $\mathbf{A}^\# \delta \mathbf{b}$, caused by the small singular values of \mathbf{A} . The optimal choice for the regularization parameter, λ , for a given problem is then a value in which the two error components are balanced forming the basis for parameter selection techniques such as the discrepancy principal, GCV and L-curve criterion (Hansen 2002).

In limited-data tomography problems, however, the system is inherently rank-deficient and indeterminate in nature. Since very few discretized pixels are transected by beams, the addition of $\mathbf{Lx} = 0$ relates the attenuation measurements from the sampled elements to the surrounding un-sampled elements. In this sense, the Tikhonov regularization equations become integral in the problem physics rather than simply used to suppress noise amplification. Daun (2010) showed that due to the relatively large m non-trivial singular values of the kernel \mathbf{A} , the reconstructed solutions are relatively stable to perturbation error over a large range of λ . As a result, the perturbation error, $\mathbf{A}^\# \delta \mathbf{b}$, is negligible.

As mentioned above, with an ill-posed full-rank problem obtaining an optimal resolution matrix, $\mathbf{R} = \mathbf{I}$, is mathematically possible leading to no regularization error. Unfortunately, the rank-deficiency of \mathbf{A} mandates the use of $\mathbf{Lx} = 0$, forcing the off-diagonal values of \mathbf{R} to be non-zero as the estimated solution values are geometric weighted averages of neighbouring pixels (Berryman 1994). Since the regularization matrix, \mathbf{L} , is defined and fixed for the problem, the resolution matrix is in turn only a function of the beam arrangement specifications in \mathbf{A} , i.e. $\mathbf{R}(\Phi) = \mathbf{A}^\#(\Phi)\mathbf{A}(\Phi)$, where $\Phi = [\Phi_1, \Phi_2 \dots \Phi_m]^T$ is a set of $[s, \theta]$ values that specify the locations of the beams.

Since it is expected that regularization error is the most prominent form of error in the system, it stands that an optimal detection array should aim to reduce the regularization error of the system. To

reduce this component, \mathbf{R} should be as close to the identity matrix as possible, forming the basis of a novel metric to quantify the expected accuracy of a reconstruction, defined as the Frobenius norm between the resolution and identity matrices,

$$F(\Phi) = \|\mathbf{R}(\Phi) - \mathbf{I}\|_F^2 \quad (4.7)$$

which is a measure of the *resolution* of the system (Menke 1989). Through the mathematical formulation above, a beam arrangement that produces a small value of $F(\Phi)$ should correspond to low regularization error in \mathbf{x}_λ .

A contour plot of a particular beam arrangement's resolution matrix can present the concept of the proposed fitness function in a qualitative sense as well. Figure 4.4 shows a contour plot of the resolution matrices for two separate beam arrangements Figure 4.2 (a) and (d) respectively, (using a 1600 pixel reconstruction domain). From the plots below there exists a well-defined diagonal nature for in Figure 4.4 (a) whereas Figure 4.4 (b) contains many more non-zero off-diagonal values. In turn, the associated fitness values for these arrays are $F(\Phi^a) = 1825.96$ and $F(\Phi^b) = 2153.11$ for Figure 4.4 (a) and (b) respectively.

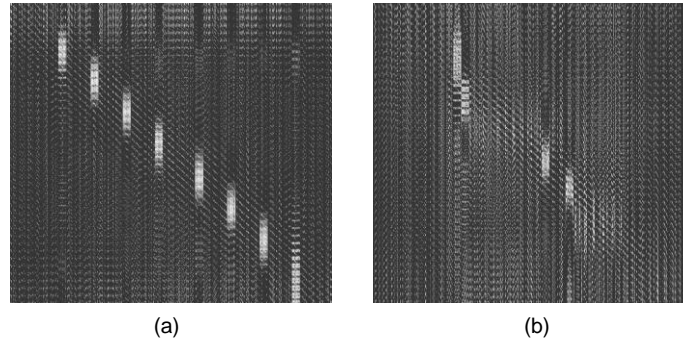


Figure 4.4 – Contour plots of resolution matrices corresponding to Figure 4.2 (a) and (d) for Figure 4.2 (a) and (b) respectively, 1600 pixel reconstruction domain

4.3 Parameter Selection

As previously mentioned in Section 2.5.2.2, the first task in conducting Tikhonov regularization methods is to select the value of the regularization parameter, λ , in Equation (2.19). Section 3.6.1 showed

how the method pioneered by Daun, predicted that a value of $\lambda = 0.05$ is sufficient to avoid the issues of oversmoothing and undersmoothing given a 1600 pixel domain.

To validate the claim that perturbation error associated with the reconstruction is negligible with respect to regularization error, a study was conducted using a simulated laser absorption experiment under both noise-free and noisy data condition for various values of λ using 1000 randomly placed Gaussian plumes as a simulation phantom. By investigating the average reconstruction error for both these cases we can further understand the optimal choice for the regularization parameter. Simulated beam attenuation data was generated using high-order numerical integration scheme and the noisy data was contaminated with normally-distributed error corresponding to a signal-to-noise ratio of 28 dB, which was reported by Garcia-Stewart et al. (2003) in publication of their laser absorption tomography experiments. An example Gaussian phantom and reconstruction are shown in Figure 4.5.

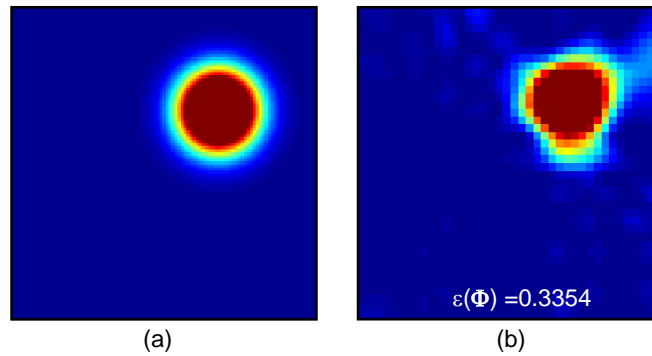


Figure 4.5 – (a) Sample Gaussian phantom, (b) Corresponding Tikhonov reconstruction and error

Figure 4.6 shows reconstruction errors of the simulation for various values of λ using the beam arrangement in Figure 4.2 (a). The result show that reconstruction error decreases with increasing λ up to $\lambda = 0.01$ as smoothing becomes more prominent in the problem physics. For larger values, $\lambda > 0.01$, the reconstruction error increases due to over-smoothing of the reconstruction.

Reconstruction error is approximately constant over an order of magnitude of λ , in contrast with full-rank discrete ill-posed problems which usually have a distinct optimum value of λ .

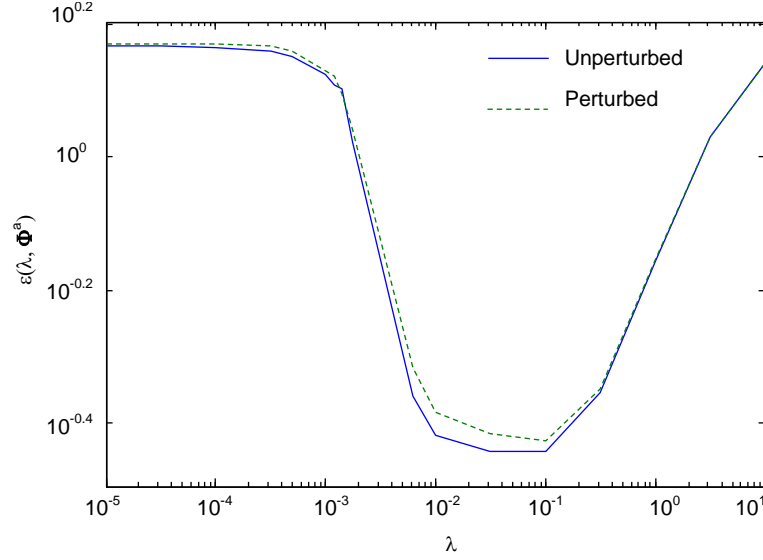


Figure 4.6 – Reconstruction error for various values of λ , using random Gaussian phantoms, 1600 pixel domain, beam arrangement 4.2 (a)

The similarity in reconstruction accuracy obtained using noised and unperturbed data reveals that perturbation error is indeed considerably smaller than regularization error. Similar studies were carried out on the other beam arrangements which all concluded that the optimal value of λ was near 0.05. Based on this result, $\lambda = 0.05$ was fixed as the regularization parameter.

4.4 Validation of Fitness Function

To validate the proposed fitness function's correlation with reconstruction error, parametric univariate studies were conducted on regular orthogonal and fan-beam arrangements. In each study, a single variable that defines detection array geometry was varied and the corresponding fitness value and reconstruction error from a simulated laser absorption experiment were compared.

The first study used a four-projection, rectilinear, regular 32-beam arrangement as a basic design as shown in Figure 4.2 (a). The adjacent beam spacing, ω , shown in Figure 4.7, for all projections was linearly varied between minimum (all beams very close) and maximum (most outward beams at edge of domain) values. The Gaussian phantoms used in the simulated experiments were randomly located and sized within the tomography domain. Figure 4.7 shows the correlation between fitness and reconstruction

error versus the parallel beam spacing. These results verify that $F(\Phi)$ is closely-correlated with the reconstruction error of the simulated experiment.

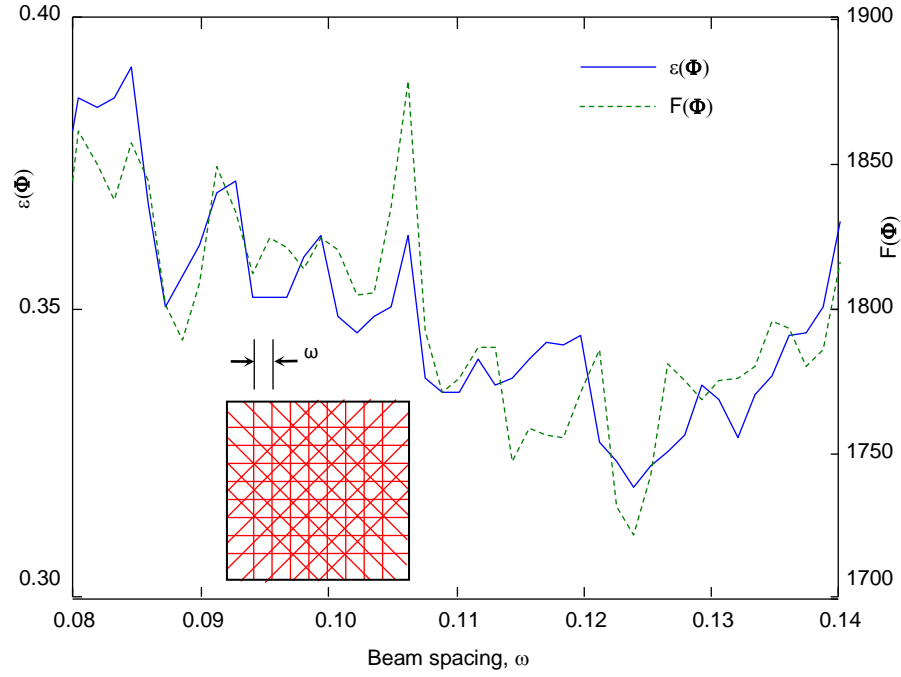


Figure 4.7 – Fitness function and reconstruction error for regular beam arrangement for various beam spacings

The second study involved the use of a 3-projection 33-beam fan arrangement, like that of Figure 4.2 (b), in which the spread angle of the projections, α , shown below in Figure 4.8, was linearly varied. This plot shows an excellent agreement between the two terms and displays an immediate relationship between the proposed fitness function and the reconstruction error of a noise-free data system, i.e. perturbation error is zero.

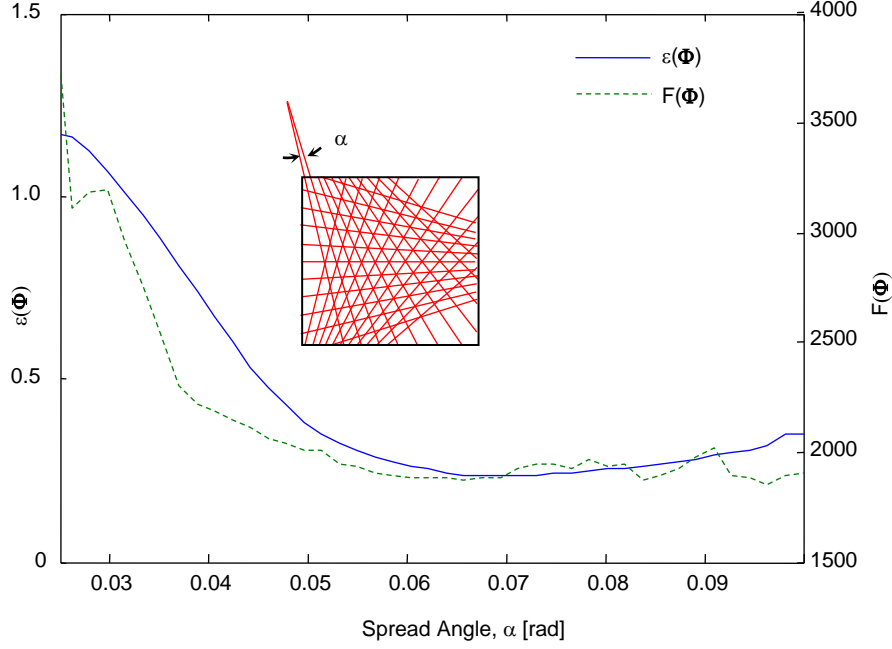


Figure 4.8 – Fitness function and reconstruction error for fan beam arrangement with various values of spread angle

4.5 Genetic Algorithms and Beam Arrangement Optimization

The fitness function is now used as a basis for beam arrangement optimization. Using Equation (4.7), the beam arrangement optimization problem is rewritten as a multivariate non-linear minimization problem,

$$\Phi^* = \arg \min [F(\Phi)] \quad (4.8)$$

for an array of m beams, $\Phi \in \mathbb{R}^{2 \times m}$, where Φ^* is the optimized beam arrangement.

Initial attempts to solve an unconstrained 32-beam arrangement optimization were made using the gradient descent based quasi-Newton method. However, the problem topology was shown to be extremely multimodal, and consequently gradient-based methods are not well suited for this type of search space as the algorithm quickly finds a local minimum near the initial conditions and terminates.

To overcome the difficulties associated with the multimodal non-linear problem, metaheuristic search algorithms, such as genetic algorithms, are used to more effectively explore the search space.

Metaheuristic algorithms incorporate some mechanisms to allow random uphill movement in the optimization function topology to avoid getting caught in a shallow local minimum (Iglesias 2005).

Genetic algorithms were selected as a search strategy for the minimization of $F(\Phi)$. Inspired by natural selection in nature, genetic algorithms are a well-proven multi-variable search algorithm. The method is based on the generate-and-test model in which an initial population of N candidate solutions are generated using either some initial guesses or random numbers and tested for their fitness via some function, in our case calculation of Equation (4.7) (Haupt 2004). A selection process then determines which individuals of the population will be chosen to reproduce a new generation of N candidate solutions. Typically the selection process chooses the top K , termed the *elite count*, individuals based on their fitness ranking but other stochastic methods are commonly used. The elite individuals are then mated by a *crossover* process in which elements of each solution, called *chromosomes*, are combined to produce an offspring that contains characteristics of the two, or more, parents (Iglesias 2005). Genetic algorithms and their reliance on random numbers used in crossover and mutation processes means the process is non-deterministic as the same algorithm may produce a new near-global minimum for separate runs of the same algorithm (Haupt 2004, Iglesias 2005). A schematic of the genetic algorithm is shown in Figure 4.9.

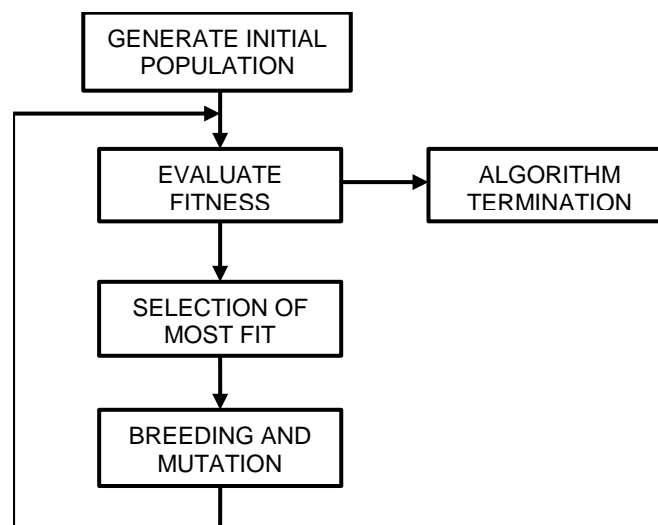


Figure 4.9 – General genetic algorithm flow chart

The first attempt at optimization considered an unconstrained $m=32$ beam irregular arrangement in which beam can possess any location within the tomography domain, resulting in 64 design parameters in the optimization. In this problem, each row of a candidate solution, $\Phi_i=[s_i, \theta_i]^T$, specifying the location of the i^{th} beam of the candidate arrangement, represents a chromosome for crossover. A population size of 500 was selected for each generation, which was found to adequately sample the search space, and an elite count of 6 was used for selection. The initial population was generated using random numbers ranging from the acceptable minimum and maximum values of each variable, i.e. $s \in [-R, R]$ where R is the width of tomography domain and $\theta \in [0, \pi]$.

The optimization was implemented using the Genetic Algorithm Solver provided in the Global Optimization Toolbox of Matlab 2010b. The scattered crossover method was chosen for reproduction in which a random binary vector containing m bits is created for each mating pair. A new offspring Φ vector is produced using the $\Phi_i=[s_i, \theta_i]^T$ pair from either parent A or parent B depending on the i^{th} bit of the random binary vector. In some cases, the offspring is mutated by randomly perturbing the elements of Φ . Mutation occurs in a relatively low number of individuals and its likelihood is governed by a probability distribution. The algorithm was run for 10 successive generations before termination, as reduction of the fitness by the best candidate between subsequent generations was found to stall after roughly 5 generations. The progress of the genetic algorithm displaying the average and best fitness of each generation is shown in Figure 4.10 (a).

The computational cost associated with the 32 beam design algorithm was approximately 7 hours using a single core of a 2 GHz i7-2630QM Intel processor with 8 GB of installed RAM. The beam arrangement corresponding to the most fit candidate, shown in Figure 4.10 (b), had a final fitness value of $F(\Phi^*)=1734.053$, smaller than the fitness values associated with the arrangements presented in Figure 4.2, $F(\Phi^a)=1824.96$, $F(\Phi^b)=1896.31$, $F(\Phi^c)=1810.98$ and $F(\Phi^d)=2153.11$ respectively.

To test the proposed optimization strategy, the accuracy of the optimized beam array was compared to those in Figure 4.2 in terms of reconstruction accuracy of a simulated laser absorption

experiment using randomly-place and sized Gaussian phantoms as in Section 4.4. The average error and for each beam arrangement and corresponding fitness value are shown in Table 4.1.

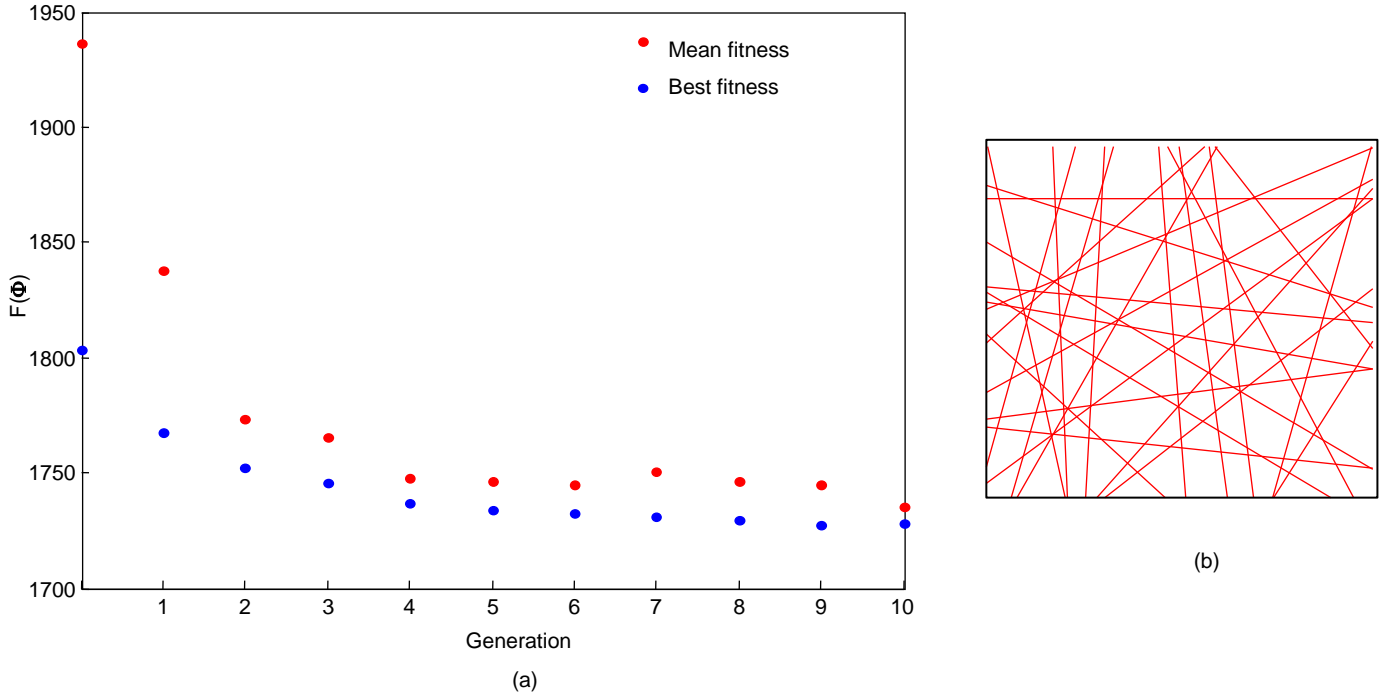


Figure 4.10 – (a) Genetic algorithm progression for 32 beam optimization, (b) Unconstrained GA optimized 32- beam arrangement

Table 4.1 – Number of beam, fitness, normalized fitness, and average error using random Gaussian phantoms for various beam arrangements

Beam Arrangement, Φ	Number of Beams, m	Fitness, $F(\Phi)$	Normalized Fitness, $F(\Phi)/m$	Average Reconstruction Error, $\varepsilon(\Phi)$
Figure 4.2 (a)	32	1824.96	57.03	0.342
Figure 4.2 (b)	33	1896.31	57.46	0.307
Figure 4.2 (c)	27	1810.96	67.07	0.420
Figure 4.2 (d)	32	2153.11	67.28	0.519
Figure 4.9 (b) (GA)	32	1734.053	54.45	0.251

For beam arrangements with a consistent number of beams, i.e. 32, the results show an excellent correlation between fitness and reconstruction error. For arrangements with different numbers of beams however, at first glance there appears to be no correlation between $F(\Phi)$ and $\varepsilon(\Phi)$. From Table 4.1, it was observed that there was a direct relation between the number of beams of an arrangement and the corresponding fitness values. In general, the fewer number of beam in the arrangement, the lower the

corresponding fitness, $F(\Phi)$. This trend is expected since the size of the problem is dependent on the number of number of unknowns, i.e. the number of beams in the candidate arrangement. Accordingly the fitness values were normalized by the number of beams, m , as shown in Table 4.1. After normalizing the fitness values, the correlation with reconstruction error was much more prominent as shown graphically in Figure 4.11.

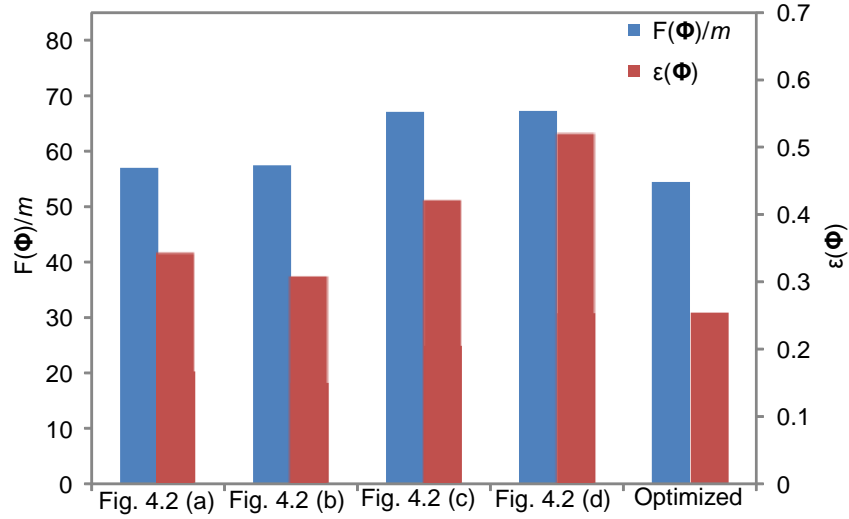


Figure 4.11 – Error and normalized fitness comparison of beam arrangements using random Gaussian phantoms

In the formulation of the proposed fitness function, Equation (4.7), each unknown pixel in the domain is treated of equal importance, as each pixel's corresponding row in the resolution matrix is compared the that of the identity matrix. In this sense, testing the GA optimized arrangement for accuracy using a randomly-placed phantom that can occur anywhere in the domain may play to the strengths of the optimized array. Also, the since the phantoms used were Gaussian functions, the smoothness *a priori* knowledge is exactly satisfied by the phantom.

To validate the findings summarized in Table 4.1 for a more realistic phantom, an additional simulation was performed using a large eddy simulation (LES) of the buoyant turbulent methane plume as the simulated phantoms, which was used previously in Section 3.6. This phantom, in contrast to the random Gaussian phantom, is primarily active toward the center of the tomographic domain and due to

the turbulent eddies in the simulated flow, concentration profile discontinuities often occur in an instantaneous image. The results for 500 of the LES phantoms are shown in Table 4.2.

Table 4.2 – Number of beam, fitness, normalized fitness, and average error using LES phantom for various beam arrangements

Beam Arrangement, Φ	Number of Beams, m	Fitness, $F(\Phi)$	Normalized Fitness, $F(\Phi)/m$	Average Reconstruction Error, $\varepsilon(\Phi)$
Figure 4.2 (a)	32	1824.96	57.03	0.441
Figure 4.2 (b)	33	1896.31	57.46	0.488
Figure 4.2 (c)	27	1810.96	67.07	0.503
Figure 4.2 (d)	32	2153.11	67.28	0.684
Figure 4.9 (b) (GA)	32	1734.053	54.45	0.388

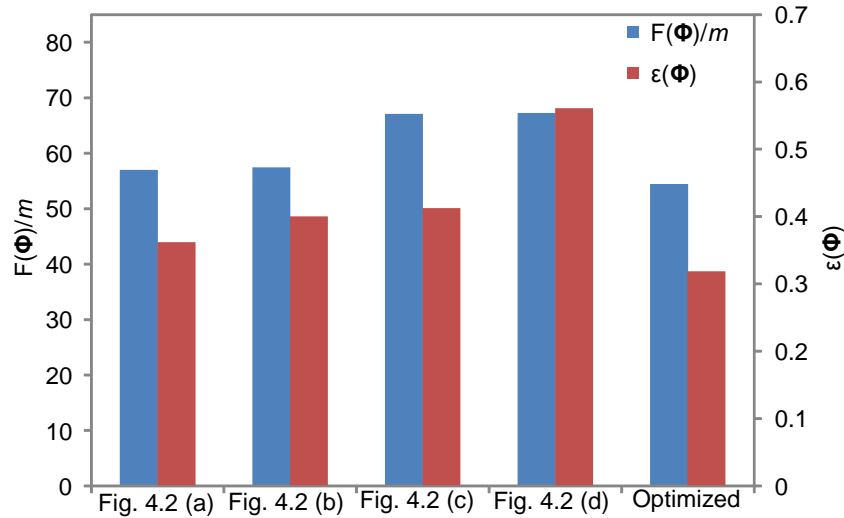


Figure 4.12 - Error and normalized fitness comparison of beam arrangements using LES phantom

Figure 4.12 shows that, similar to the results from the Gaussian phantoms, the GA optimized arrangement has superior reconstruction accuracy than all other arrangements tested. Table 4.1 and Table 4.2 show that the relative reconstruction error between the two phantom types is higher for the LES phantom. This increase in error is due to the discrepancy between the turbulent flow artifacts that arise in the LES phantom and the smoothness prior that attempts to produce a continuously-varying 2D concentration profile. A sample LES phantom image with corresponding reconstructions and error values for each of the tested beam arrangements is shown in Figure 4.13.

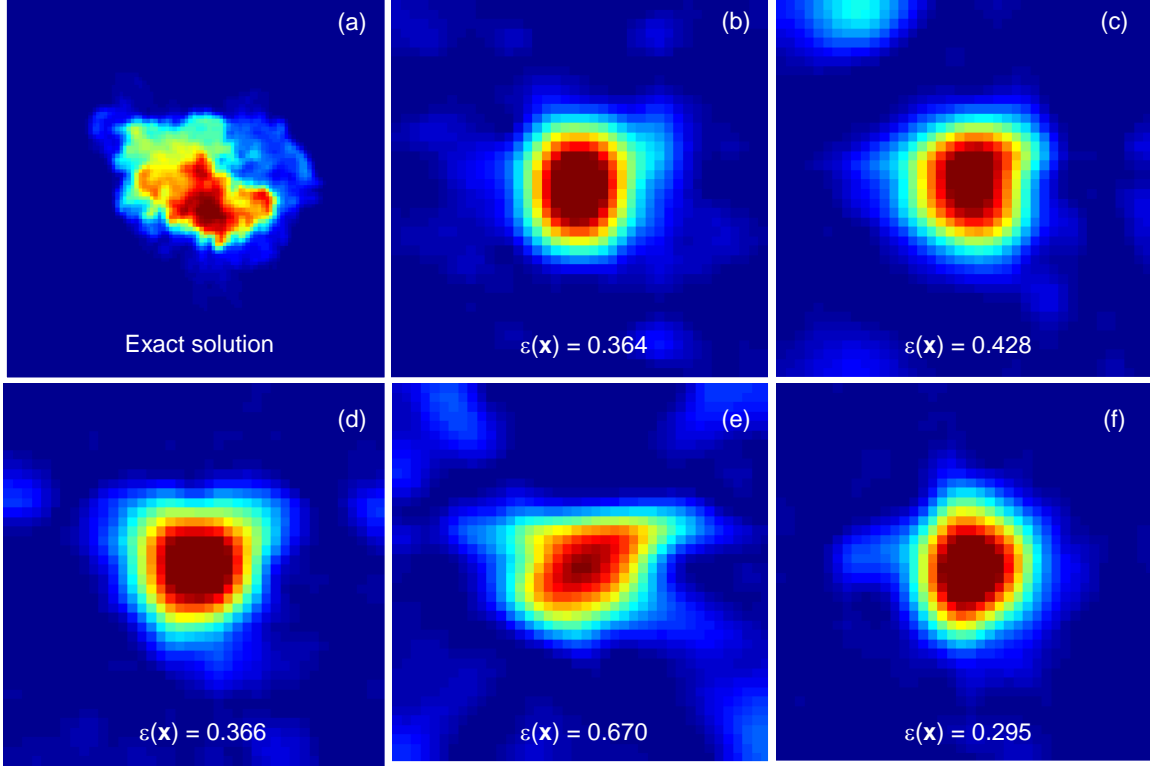


Figure 4.13 – Sample LES phantom and reconstructed concentration profiles for various beam arrangements: (b) for Figure 4.2 (a), (c) for Figure 4.2 (b), (d) for Figure 4.2 (c), (e) for Figure 4.2 (d), and (f) Figure 4.10

4.6 Effects of Beam Misalignment

In a simulation environment for performing CST experiments, the kernel matrix, \mathbf{A} , is generated from the specified beam locations relative to the discretized domain. Therefore, in simulations, the values of the \mathbf{A} matrix and the pixels sampled during attenuation are in exact agreement. In actual implementation, however, the location of the actual lasers and detectors are subject to some uncertainty based on the precision of instrument installation. These slight equipment misalignments create an inconsistency between the pixels specified in \mathbf{A} and those sampled to produce the attenuated data in \mathbf{b} , which, in turn, can lead to additional errors in the reconstruction.

To quantify the effect of experimental beam misalignment, a simulated experiment was performed in which the laser path coordinates, $[s_i, \theta_i]$, were perturbed to represent installation error while the values of the \mathbf{A} matrix remain constant. The modified beam locations were then used to sample the attenuated pixels using high-order integration.

The beam coordinates were perturbed by sampling an un-biased normal distribution centered about each of the original coordinates using $\sigma_s = 0.025$ (1/40th the width of the square tomography domain) for the standard deviation of the s parameter and $\sigma_\theta = 0.25^\circ$ (0.004363 rad) for the beam angle, which represent a realistic worst-case scenario for precision of optical components in an experimental setting. Using 1000 random Gaussian phantoms, as in Section 4.5, a simulated experiment was performed using 50 perturbed arrangements of the four beam arrangements from literature in Figure 4.2 and the optimized arrangement shown in Figure 4.10 (b). The average error and reconstruction error standard deviation is shown along with the unperturbed simulation results for comparison in Table 4.3.

Table 4.3 – Average reconstruction error for original and misaligned beam arrangements using random Gaussian phantoms

Beam Arrangement, Φ	Unperturbed Arrangement Error	Perturbed Arrangement Error	Absolute Relative Error Increase
Figure 4.2 (a)	0.342	0.37 ± 0.013	8.19%
Figure 4.2 (b)	0.307	0.33 ± 0.014	7.49%
Figure 4.2 (c)	0.420	0.43 ± 0.011	2.38%
Figure 4.2 (d)	0.519	0.54 ± 0.015	4.05%
Figure 4.9 (b) (GA)	0.251	0.28 ± 0.009	11.53%

It was found that the increase in error due to beam misalignment varied for each of the arrangements, but was generally negligible compared to the relative error between arrangements. The results were not surprising since misalignment error is essentially an additional form of data noise equivalent to perturbing values in the measurement data, **b**. It was shown that using the Tikhonov method, the m non-trivial singular values were large enough such that reconstructions were relatively robust to the effects of induced data noise over a large range of λ , and thus perturbation error is well-handled by the reconstruction algorithm.

4.7 Effect of Number of Beams on Reconstruction Accuracy

Though the arrangement of the finite number of laser/detector pairs has been shown to greatly influence the accuracy of a CST experiment, the number of attenuation measurements, m , has also had a very pronounced effect on the reconstruction. Accounting for the cost and complexity of the lasers,

collection optics, and data acquisition systems, it is essential to assess the number of beams needed to reconstruct the species concentration to a desired level of accuracy since additional beams can lead to unnecessary additional costs. However, without the ability to separate the effects of the two factors of arrangement and number of beams, little work has been done to quantify the effect the latter on reconstruction accuracy. Using the resolution fitness formulation, however, for the first time this effect can be explained.

To attempt to quantify this effect, a beam arrangement optimization using genetic algorithms (as in Section 4.5) was performed for arrangements with the number of beams ranging from $m = 8 \dots 65$ for a 1600 pixel reconstruction domain. The same procedure outlined in Section 4.5 was used to create an arrangement for each number of beams. The normalized fitness, $F(\Phi)/m$, and reconstruction error for 500 randomly-placed Gaussian phantoms, $\varepsilon(\Phi)$, is plotted against the corresponding number of beams for each case in Figure 4.14.

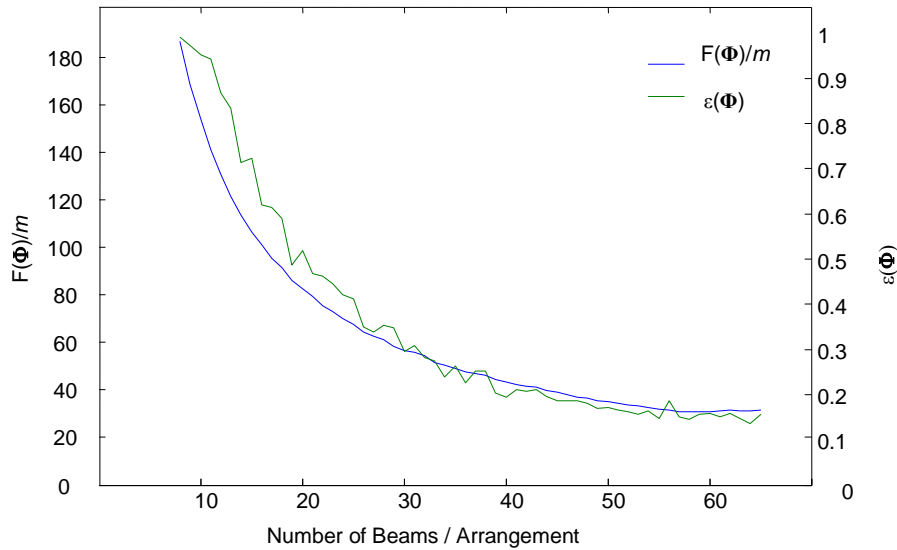


Figure 4.14 – Normalized fitness and error for various values of m using random Gaussian phantoms

Several comments can be made about the influence of Figure 4.14. First, the plot clearly displays the excellent correlation between the normalized fitness and reconstruction error, further validating the proposed fitness function. Second, it appears that both trends in Figure 4.14 are asymptotic in nature,

where there is a very steep reduction in error and fitness from $m = 8$ –20, followed by a less significant reduction thereafter. Using the plot above, an experimentalist can visualize the benefit of additional beams on the reconstruction accuracy. By performing analysis on such a curve, based on the local slope, a designer can decide when improvement is incremental based on added equipment costs. To the best of the author’s knowledge, this is the first attempt to model and quantify the effects of the number of beams used in the arrangement on the accuracy of a CST experiment. Note that the plot created in Figure 4.14 is specific to the domain shape and discretization, so the trends may change based on the number of pixels used in the reconstruction.

4.8 Constrained Arrangement Optimization for FLITES Project

Section 4.5 outlined a beam arrangement optimization for an unconstrained problem in which the laser/detector pairs could have any location, and thus the beams can be anywhere in the domain. In practice however, restrictions are imposed based on the physical space of the problem and the ability to access these areas, such as the IC engine tomography system developed at the University of Manchester previously discussed in Section 2.5. In these types of problems, the optimized solution conforms to physical constraints of the problem.

To test the proposed optimization method on a constrained problem geometry, optimizations of a large-scale tomography problem were done in conjunction with researchers at the University of Manchester regarding the on-going FLITES project. The FLITES (Fibre-Laser Imaging of Turbine Exhaust Species) project is an industrial-academic effort including members from Rolls-Royce, Shell, Covision, Fianium, OptoSci, and the Universities of Southampton and Strathclyde aimed at monitoring the chemical species emission, namely CO_2 and unburned hydrocarbons (UHCs), from a full-scale aerospace turbine through the design of a CST system. One of the main hurdles of the project was determining how to arrange the 126 attenuating lasers across the 6 m diameter annulus bounded by the predetermined circular launch and receive mounting frame. A reconstruction domain was set by

researchers at the University of Manchester as 70×70 over a 1.6 m square centered at the axis of symmetric of the turbine. The basic experimental setup of the FLITES project is shown in Figure 4.15.

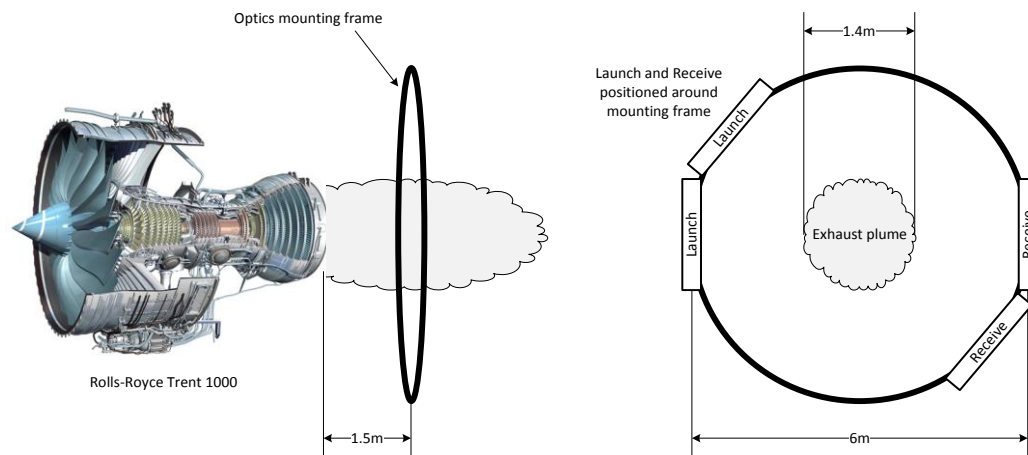


Figure 4.15 – FLITES geometric arrangement of engine and beam arrangement mounting fixture (Figure adopted from McCormick 2013)

To optimize the beam arrangement for the FLITES project, a set of constraints was first imposed based on the physical limitations and practicality of implementing the designs. The first constraint imposed was that the launch/receive optics must be positioned along the fixed circular mounting frame shown in Figure 4.15. It was also imposed that no two beams could be placed such that the laser or detectors interfered with each other, or interrupted a beam. During discussion with University of Manchester researchers, an additional, and intuitive, constraint of array symmetry with respect to the reconstruction domain was discussed to reduce the size of the optimization problem. From these constraints, five different optimization cases were formulated at request of the group at the University of Manchester, outlined in Table 4.4 below.

Table 4.4 – FLITES optimization cases and corresponding constraints

Optimization Case	Array Type	Optimization Constraints	Optimization Dimensions (Variables)
1	Regular	Fixed L/R position, single spacing for all projections	1
2	Regular	Fixed L/R position, single spacing per projections	6
3	Irregular	Fixed L/R position, variable L/R pairings	126
4	Irregular	Fixed L/R position, variable L/R pairings, projection and radial symmetry	10
5	Irregular	Variable L/R position, variable L/R pairings, projection and radial symmetry	20

Optimization Case 1 and Case 2 use the framework of a 6-projection, parallel beam, regular arrangement design for the array structure, like that of Figure 4.2 (a). In Case 1, each of the 6 projections contains a single parallel beam spacing which can vary between minimum and maximum spacing constrained by the size of the launch/receive optics and 1.6 m domain respectively. This case is a univariate optimization problem and maximum variable value is given, the optimization can be performed through a parametric study, as in Section 4.4.

Case 2 is very similar to that of Case 1 except that each of the 6 projection can possess its own individual beam spacing, increasing the search space of the problem. The increased problem dimension leads to the use of genetic algorithms for the optimizations of Cases 2-5.

Optimization Cases 3-5 are examples of irregular arrays. In these problems, the position of the launch/receive optics are fixed in location (or can be slightly modified) as specified by researchers at the University of Manchester.

In Optimization Case 3, each launch location (fixed and predefined) is able to choose any of the 126 receive locations anywhere along the mounting structure as a “mate”. In this optimization there are 126 variables to be specified.

Optimization Case 4 is very similar to Case 3 except that the launch and receive pairings are only specified and variable for one of the 6 projections. Each projection must also be symmetric with respect to the individual projection. The specification for the single projection is then mirrored on each of the 6

projections. In this optimization the optimization dimension is significantly reduced by imposing the domain symmetric, creating a 10 variable optimization.

The final optimization, Optimization Case 5, uses the exact same constraints as Case 4 except for the fact that each of the fixed launch/receive locations can be slightly modified so long as that the components are not in physical interference. This additional factor is accomplished by allowing the location of each component to be specified within a given positional range along the mounting structure, resulting in an optimization dimension twice that of Case 4, 20 variables. Each of the GA optimizations used a population size of 1000 individuals, an elite count of 20 and was allowed to proceed for 5 generations using a procedure similar to that outline in Section 4.5. The optimized results along with the process of each of the optimizations are shown in Figure 4.18.

Each of the optimization results was tested using a simulated experiment using an approximation of an exhaust plume as the phantom. The phantom consisted of an annulus of 18 2D Gaussian functions to represent the combustion products of the 18 burners of the aerospace engine to be investigated. The phantom and reconstruction for each optimized arrangement is shown in Figure 4.16.

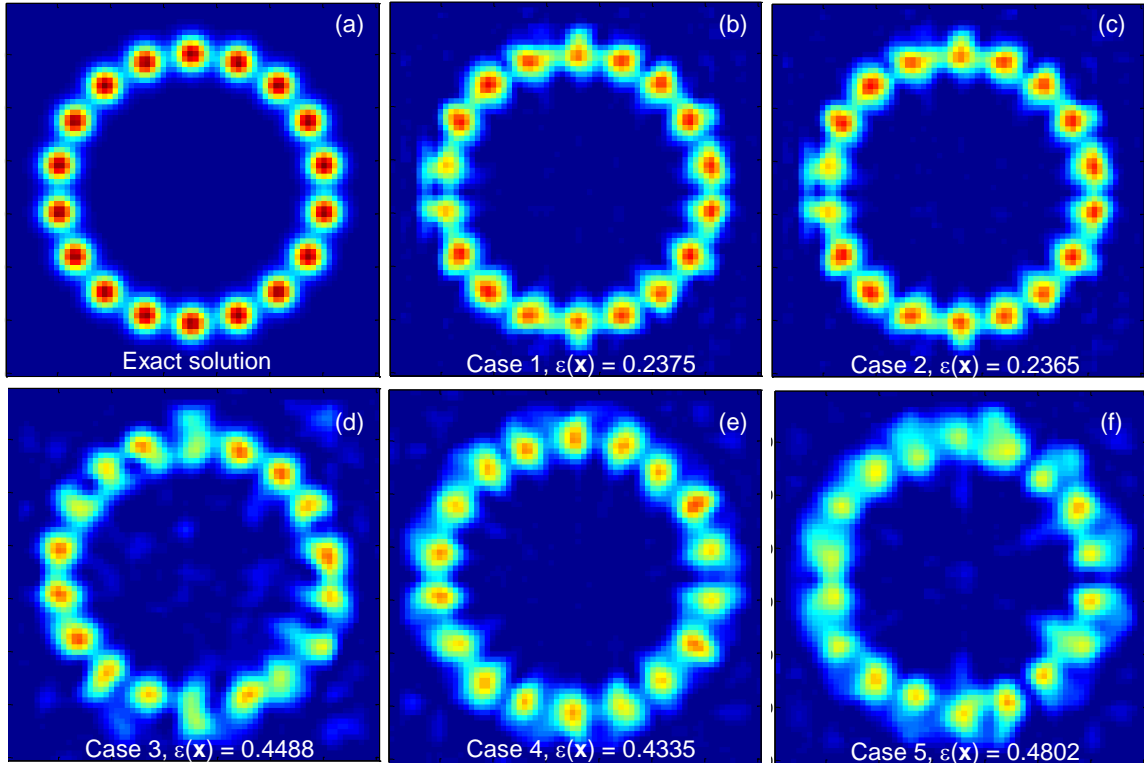


Figure 4.16 - Reconstruction results and corresponding error for each optimized case

Comparing the relative fitness and reconstruction error of each arrangement again displays the relationship between $F(\Phi)$ and $\varepsilon(\Phi)$, as shown in Figure 4.17.

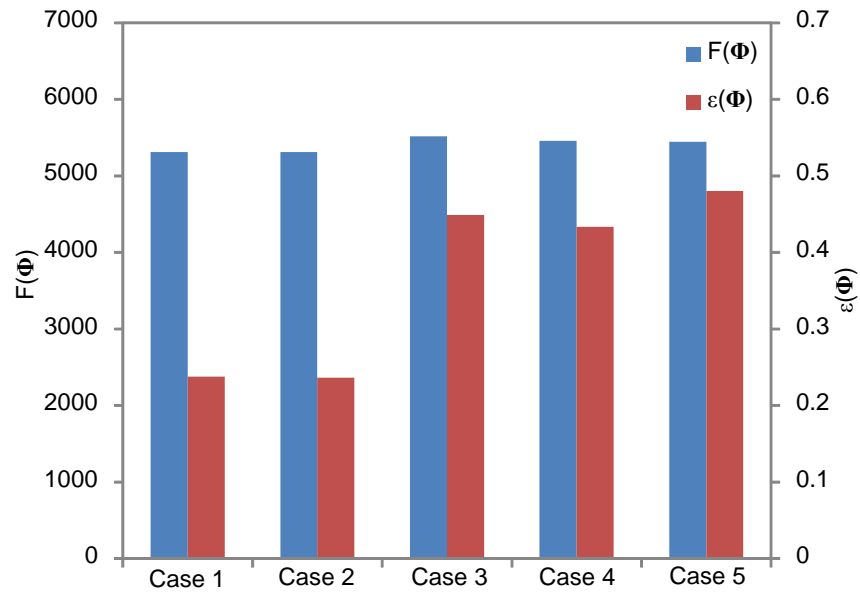


Figure 4.17 – Fitness and reconstruction error for each optimization case

Figure 4.17 shows that the regular arrays, Optimization Case 1 and Optimization Case 2, display superior fitness and reconstruction accuracy compared to the irregular optimization cases. The figures also show that the regular array optimizations converged to the same solutions, maximizing the spread of the parallel beam spacing for each projection. From the results it can be concluded that the regular arrays provide better reconstruction results, which is evident from the reconstructions shown in Figure 4.16, as the regular arrays possess less than half the reconstruction error of the irregular arrays. The reason for the poor performance of the irregular arrays is the limitations and constraints imposed on each of the optimizations as well as the increased search space size in each of the optimizations for the same amount of search time. For example, it is conceivable that Optimization Case 3 could converge toward a regular ray design, but due to the metaheuristic nature of the genetic algorithms and the fact that the search space has 21 times as many variables to optimize, the algorithm simply not given enough search time to find the regular solution. Therefore, for the given set of constraints, the regular array design is best suited for the tomography problem in question. By observing the arrangements themselves, this conclusion is intuitive as the regular array seems to sample the domain much more uniformly.

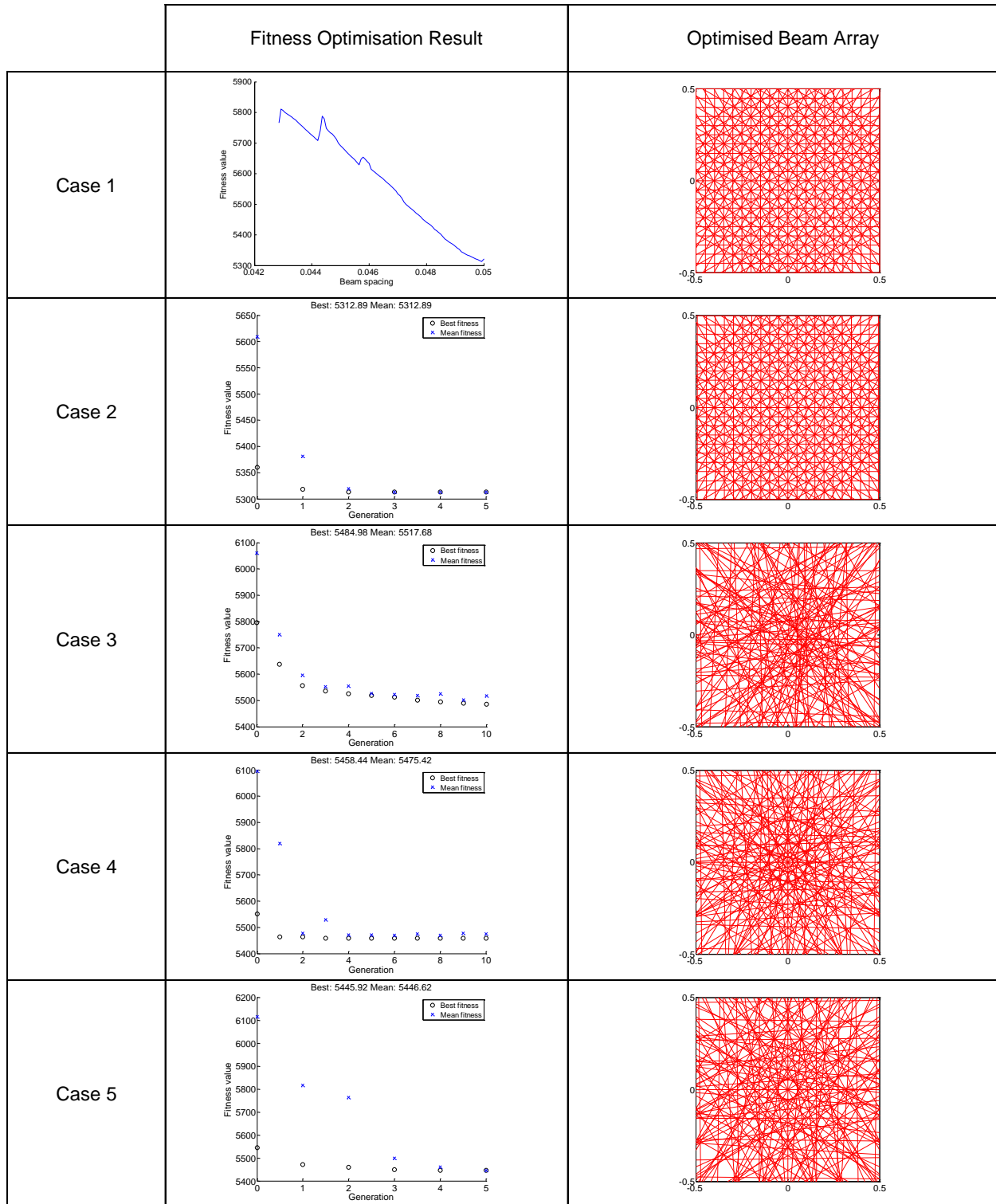


Figure 4.18 – Genetic algorithm progressions and optimized beam array for each optimization case

5. CONCLUSIONS AND FUTURE WORK

5.1 Conclusions

This thesis describes two innovations relating to the accuracy of laser absorption chemical species tomography experiments. Chapter 3 discussed a novel solution prior of a contiguous concentration profile which can further decrease the tomographic reconstruction error by being incorporated into the solution algorithm. Using the level set method, the well-defined interface between the species of interest and co-flow can be modelled and iteratively deformed from a signed distance function by the influence of the measurements to produce a solution that explains the attenuation data and is consistent with other *a priori* information of smoothness and non-negativity. The level set reconstruction algorithm is shown to create more accurate solution than first-order Tikhonov reconstructions because the algorithm permits solutions with localized regions of smoothness regularization rather than throughout the entire domain which leads to smearing artifacts.

Chapter 4 investigates the correlation between resolution matrices, formed by the subtended chords lengths of the beams in each domain pixel, and reconstruction error of limited data tomography experiments. Using resolution matrices it is possible to relate the reconstructed results to the exact solution independent of the actual gas concentration distribution. Using this relation, beam arrangements can be optimized with respect to a fitness function using a genetic algorithm. This design methodology was demonstrated by optimizing an unconstrained array of 32 beams. The reconstruction accuracy obtained using this optimized configuration is superior to other arrangements presented in literature. The optimization process was also conducted on a real-world design case containing a set of physical constraints. The effects of beam misalignment were investigated, which was found to have negligible effect. The trade-off between the number of beams used in the arrangement, m , and reconstruction error, ϵ , was visualized by comparing the accuracy of optimized beam arrays containing various numbers of beams.

5.2 Future Work

5.2.1 Level Set Method Algorithm Parameters and Initial Conditions

Regularization parameter selection methods are very important for determining the proper level of regularization to impose on an ill-posed system. Methods such as the SVD-related process used by Daun mathematically derive acceptable values of λ for Tikhonov reconstructions that avoid the complications of oversmoothing and undersmoothing. Without such methods, reconstruction algorithm designers must resort to the use of heuristics to choose optimal values. Such is the case with the level set reconstruction method outlined in Chapter 3. Though the regularization parameter μ_1 is bounded as specified by the CFL condition, future work involving the tomographic level set method reconstruction should investigate parameter selection techniques to effectively define values of μ_2 in Equation (3.21). Without a mathematical basis for the choice of this parameter, the applicability of the algorithm is severely limited.

A common obstacle in iterative methods such as that of the proposed level set reconstruction algorithm is the choice for the initial solution estimation, ϕ_0 . Li et al. note in their research that in iterative schemes such as the level set method the solution can have a dependence on the initial guess, ϕ_0 . The method described in Chapter 3 exclusively uses signed distance functions as initial estimations due to their associated level set method iterative stability. Future work should investigate the effect of the initial condition on the final solution as well as the use of other initial estimations, such as flat and step functions, for ϕ_0 .

While the Tikhonov and the proposed level set reconstruction methods have shown to accurately solve the limited data tomography problem, other methods have the potential to further improve tomographic solutions. Techniques based on Bayesian mathematics attempt to maximize the posterior probability of a problem based on experimental observations and given *a priori* knowledge. The robustness of Bayes' framework allows the incorporation of more advanced priors including those arising from turbulent statistical theory and also allows for the quantification of uncertainty in the recovered solution. Additionally, metaheuristic techniques, such as neural networks, bypass the need to explicit *a*

priori knowledge through machine learning. In these methods, an algorithm is given both the experimental and the exact solution, attempting to construct a mathematical system that relates the two variables (Warsito 2001). Future work should investigate the use of these methods for design of the next generation of tomographic reconstruction algorithms.

5.2.2 Resolution Matrices and Optimization

As mentioned previously in Section 4.5, the formulation of the fitness function, Equation (4.7), means that each pixel in the reconstruction domain is of equal importance. In some cases however, there exist specific areas of the domain in which resolution is more desirable, areas of interest. By modifying the formulation of the fitness function, particular areas of the domain can be weighted as more important in terms of the reconstruction resolution, and thus optimizations taking into account these areas can be conducted. By inserting a weighting matrix, \mathbf{W} , into Equation (4.7),

$$F(\Phi) = \|\mathbf{W} \cdot \mathbf{R}(\Phi) - \mathbf{I}\|_F^2 \quad (4.9)$$

where $\mathbf{W} = \text{diag}(W_1, \dots, W_n)$ is a diagonal positive real-valued matrix, areas of the domain can be deemed unimportant, i.e. $0 < W_i < 1$, or an area of interest for the reconstruction's expected regions of detection, i.e. $W_i > 1$. Future work in resolution matrices for tomographic applications should investigate the concept of weighted resolution matrices and their effect in weighted array optimizations.

Since genetic algorithms are a metaheuristic method, for highly multimodal problems the optimized solutions are inherently non-deterministic. As such, optimization of a tomographic detection array can lead to different results for successive runs of the same algorithm. Future work in beam arrangement optimization should explore alternative search schemes in an effort to find the global minimum of a resolution fitness function search space given a set of design constraints.

6. REFERENCES

- Åkesson, E. O., & Daun, K. J. (2008). Parameter selection methods for axisymmetric flame tomography through Tikhonov regularization. *Applied optics*, 47(3), 407-416.
- Beiting, E. J. (1992). Fiber-optic fan-beam absorption tomography. *Applied optics*, 31(9), 1328-1343.
- Berryman, J. G. (1994, September). Tomographic resolution without singular value decomposition. In *SPIE's 1994 International Symposium on Optics, Imaging, and Instrumentation* (pp. 2-13). International Society for Optics and Photonics.
- Bertero, M., & Boccacci, P. (1998). *Introduction to inverse problems in imaging*. CRC press.
- Budinger, T. F., Gullberg, G. T., & Huesman, R. H. (1979). Emission computed tomography. In *Image reconstruction from projections* (pp. 147-246). Springer Berlin Heidelberg.
- Cai, W., Ewing, D. J., & Ma, L. (2008). Application of simulated annealing for multispectral tomography. *Computer Physics Communications*, 179(4), 250-255.
- Carey, S. J., McCann, H., Winterbone, D. E., & Clough, E. (1999). Near infra-red absorption tomography for measurement of chemical species distribution. In *1st World Congress on Industrial Process Tomography* (Vol. 487). Buxton: Greater Manchester.
- Carey, S. J., McCann, H., Hindle, F. P., Ozanyan, K. B., Winterbone, D. E., & Clough, E. (2000). Chemical species tomography by near infra-red absorption. *Chemical Engineering Journal*, 77(1), 111-118.
- Cessou, A., Meier, U., & Stepowski, D. (2000). Applications of planar laser induced fluorescence in turbulent reacting flows. *Measurement Science and Technology*, 11(7), 887.
- Chu, P. C., Lee, J. H., & Chu, V. H. (1999). Spreading of turbulent round jet in coflow. *Journal of Hydraulic Engineering*, 125(2), 193-204.
- Crosson, R. S. (1976). Crustal structure modeling of earthquake data: 1. Simultaneous least squares estimation of hypocenter and velocity parameters. *Journal of geophysical research*, 81(17), 3036-3046.

- Curtis, A. (1999). Optimal experiment design: cross-borehole tomographic examples. *Geophysical Journal International*, 136(3), 637-650.
- Daun, K. J. (2010). Infrared species limited data tomography through Tikhonov reconstruction. *Journal of Quantitative Spectroscopy and Radiative Transfer*, 111(1), 105-115.
- Daun, K. J., Waslander, S. L., & Tulloch, B. B. (2011). Infrared species tomography of a transient flow field using Kalman filtering. *Applied Optics*, 50(6), 891-900.
- Davidson, M. J., & Wang, H. J. (2002). Strongly advected jet in a coflow. *Journal of Hydraulic Engineering*, 128(8), 742-752.
- Eckbreth, A. C., Anderson, T. J., & Dobbs, G. M. (1988). Multi-color CARS for hydrogen-fueled scramjet applications. *Applied Physics B*, 45(4), 215-223.
- Edwards, B. N., & Burch, D. E. (1965). Absorption of 3.39-Micron Helium—Neon Laser Emission by Methane in the Atmosphere. *JOSA*, 55(2), 174-177.
- Garcia-Stewart, C. A., Polydorides, N., Ozanyan, K. B., & McCann, H. (2003, September). Image reconstruction algorithms for high-speed chemical species tomography. In *Proceedings of 3rd World Conference on Industrial Process Tomography (Virtual Centre for Industrial and Process Tomography, 2003)* (pp. 80-85).
- Gazzah, M. H., Boughattas, N., Belmabrouk, H., & Said, R. (2010). The dynamic field in turbulent round jet discharging into a co-flowing stream. *energy*, 10, 6.
- Gilboa, G., Sochen, N., & Zeevi, Y. Y. (2002). Forward-and-backward diffusion processes for adaptive image enhancement and denoising. *Image Processing, IEEE Transactions on*, 11(7), 689-703.
- Hadamard, J. (1923). *Lectures on Cauchy's Problem in Linear Partial Differential Equations*. New York: Yale University Press.
- Hansen, P. C. (1990). Truncated singular value decomposition solutions to discrete ill-posed problems with ill-determined numerical rank. *SIAM Journal on Scientific and Statistical Computing*, 11(3), 503-518.

- Hansen, P. C. (1992). Analysis of discrete ill-posed problems by means of the L-curve. *SIAM review*, 34(4), 561-580.
- Hansen, P. C. (1998). Rank-deficient and discrete ill-posed problems: numerical aspects of linear inversion (Vol. 4). Siam.
- Hanson, R. K., Seitzman, J. M., & Paul, P. H. (1990). Planar laser-fluorescence imaging of combustion gases. *Applied Physics B*, 50(6), 441-454.
- Haupt, R. L., & Haupt, S. E. (2004). *Practical genetic algorithms*. John Wiley & Sons.
- Hindle, F. P., Carey, S. J., Ozanyan, K., Winterbone, D. E., Clough, E., & McCann, H. (2001). Measurement of gaseous hydrocarbon distribution by a near-infrared absorption tomography system. *Journal of Electronic Imaging*, 10(3), 593-600.
- Ho, S., Bullitt, E., & Gerig, G. (2002). Level-set evolution with region competition: automatic 3-D segmentation of brain tumors. In *Pattern Recognition, 2002. Proceedings. 16th International Conference on* (Vol. 1, pp. 532-535). IEEE.
- Ibrahim, S., Green, R. G., Dutton, K., Evans, K., Rahim, R. A., & Goude, A. (1999). Optical sensor configurations for process tomography. *Measurement Science and Technology*, 10(11), 1079.
- Iglesias, M. T. (2005). *Foundations of generic optimization* (Vol. 2). R. Lowen, & A. Verschoren (Eds.). Springer.
- Incropera, F. P., Lavine, A. S., & DeWitt, D. P. (2007). *Fundamentals of heat and mass transfer*. John Wiley & Sons Incorporated.
- Javed, M. T., Irfan, N., & Gibbs, B. M. (2007). Control of combustion-generated nitrogen oxides by selective non-catalytic reduction. *Journal of Environmental Management*, 83(3), 251-289.
- Klingbeil, A. E., Jeffries, J. B., & Hanson, R. K. (2006). Temperature-and pressure-dependent absorption cross sections of gaseous hydrocarbons at 3.39 μm . *Measurement Science and Technology*, 17(7), 1950.
- Landweber, L. (1951). An iteration formula for Fredholm integral equations of the first kind. *American journal of mathematics*, 73(3), 615-624.

- Lees, J. M., & Crosson, R. S. (1989). Tomographic inversion for three-dimensional velocity structure at Mount St. Helens using earthquake data. *Journal of Geophysical Research: Solid Earth (1978–2012)*, 94(B5), 5716-5728.
- Li, C., Xu, C., Gui, C., & Fox, M. D. (2005, June). Level set evolution without re-initialization: a new variational formulation. In *Computer Vision and Pattern Recognition, 2005. CVPR 2005. IEEE Computer Society Conference on* (Vol. 1), pp. 430-436.
- Li, C., Xu, C., Gui, C., & Fox, M. D. (2010). Distance regularized level set evolution and its application to image segmentation. *Image Processing, IEEE Transactions on*, 19(12), 3243-3254.
- Litman, A., Lesselier, D., & Santosa, F. (1998). Reconstruction of a two-dimensional binary obstacle by controlled evolution of a level-set. *Inverse problems*, 14(3), 685.
- Liu, C., Xu, L., Cao, Z., & Yang, Y. (2012, July). Fan-beam TDLAS tomography for gas concentration distribution with limited data. In *Imaging Systems and Techniques (IST), 2012 IEEE International Conference on* (pp. 117-120). IEEE.
- Ma, L., & Cai, W. (2008). Determination of the optimal regularization parameters in hyperspectral tomography. *Applied optics*, 47(23), 4186-4192.
- Ma, L., & Cai, W. (2008). Numerical investigation of hyperspectral tomography for simultaneous temperature and concentration imaging. *Applied optics*, 47(21), 3751-3759.
- Ma, L., Cai, W., Caswell, A. W., Kraetschmer, T., Sanders, S. T., Roy, S., & Gord, J. R. (2009). Tomographic imaging of temperature and chemical species based on hyperspectral absorption spectroscopy. *Optics Express*, 17(10), 8602-8613.
- Ma, L., Li, X., Sanders, S. T., Caswell, A. W., Roy, S., Plemmons, D. H., & Gord, J. R. (2013). 50-kHz-rate 2D imaging of temperature and H₂O concentration at the exhaust plane of a J85 engine using hyperspectral tomography. *Optics express*, 21(1), 1152-1162.
- MacCarthy, J. K., Borchers, B., & Aster, R. C. (2011). Efficient stochastic estimation of the model resolution matrix diagonal and generalized cross-validation for large geophysical inverse problems. *Journal of Geophysical Research: Solid Earth (1978–2012)*, 116(B10).

- McCormick, D., Twynstra, M.G., Daun, K.J., McCann, H., (2013). Optimising laser absorption tomography beam arrays for imaging chemical species in gas turbine exhaust plumes. World Congress on Industrial Tomography 2013. In press.
- Menke, W. (1989). *Geophysical data analysis: discrete inverse theory* (Vol. 45). Academic Press Inc.
- Modest, M. F., & Modest, M. F. (2003). *Radiative heat transfer* (pp. 383-437). New York: McGraw-Hill., pp. 289-291.
- Osher, S., & Fedkiw, R. (2003). *Level set methods and dynamic implicit surfaces* (Vol. 153). Springer.
- Pal, S., Ozanyan, K. B., & McCann, H. (2008). A computational study of tomographic measurement of carbon monoxide at minor concentrations. *Measurement Science and Technology*, 19(9), 094018.
- Peng, H., & Stark, H. (1987). Direct Fourier reconstruction in fan-beam tomography. *Medical Imaging, IEEE Transactions on*, 6(3), 209-219.
- Perona, P., & Malik, J. (1990). Scale-space and edge detection using anisotropic diffusion. *Pattern Analysis and Machine Intelligence, IEEE Transactions on*, 12(7), 629-639.
- Piccolomini, E. L., & Zama, F. (1999). The conjugate gradient regularization method in computed tomography problems. *Applied mathematics and computation*, 102(1), 87-99.
- Pitts, W. M. (1991). Reynolds number effects on the mixing behavior of axisymmetric turbulent jets. *Experiments in fluids*, 11(2-3), 135-141.
- Pope, S. B. (2000). *Turbulent flows*. Cambridge university press.
- Porter, J. M., Jeffries, J. B., & Hanson, R. K. (2009). Mid-infrared absorption measurements of liquid hydrocarbon fuels near. *Journal of Quantitative Spectroscopy and Radiative Transfer*, 110(18), 2135-2147.
- Rahim, R. A., Pang, J. F., & Chan, K. S. (2005). Optical tomography sensor configuration using two orthogonal and two rectilinear projection arrays. *Flow Measurement and Instrumentation*, 16(5), 327-340.

- Rothman, L. S., Gordon, I. E., Barbe, A., Benner, D. C., Bernath, P. F., Birk, M., & Vander Auwera, J. (2009). The HITRAN 2008 molecular spectroscopic database. *Journal of Quantitative Spectroscopy and Radiative Transfer*, 110(9), 533-572.
- Santoro, R. J., Semerjian, H. G., Emmerman, P. J., & Goulard, R. (1981). Optical tomography for flow field diagnostics. *International Journal of Heat and Mass Transfer*, 24(7), 1139-1150.
- Santosa, F. (1996). A level-set approach for inverse problems involving obstacles. *ESAIM: Control, Optimisation and Calculus of Variations*, 1, 17-33.
- Sussman, M., Smereka, P., & Osher, S. (1994). A level set approach for computing solutions to incompressible two-phase flow. *Journal of Computational physics*, 114(1), 146-159.
- Terzija, N., Davidson, J. L., Garcia-Stewart, C. A., Wright, P., Ozanyan, K. B., Pegrum, S., & McCann, H. (2008). Image optimization for chemical species tomography with an irregular and sparse beam array. *Measurement Science and Technology*, 19(9), 094007.
- Terzija, N., & McCann, H. (2011). Wavelet-based image reconstruction for hard-field tomography with severely limited data. *Sensors Journal, IEEE*, 11(9), 1885-1893.
- Verhoeven, D. (1993). Limited-data computed tomography algorithms for the physical sciences. *Applied Optics*, 32(20), 3736-3754.
- Warsito, W., & Fan, L. S. (2001). Neural network based multi-criterion optimization image reconstruction technique for imaging two-and three-phase flow systems using electrical capacitance tomography. *Measurement Science and Technology*, 12(12), 2198.
- Wiggins, R. A. (1972). The general linear inverse problem: Implication of surface waves and free oscillations for earth structure. *Reviews of Geophysics*, 10(1), 251-285.
- Williams, R. A., Beck, M. S. (1995). *Process tomography: principals, techniques and applications*. Elsevier.
- Wing, G. M. (1991). A primer on integral equations of the first kind: the problem of deconvolution and unfolding (No. 27). Siam.

- Wolfe Jr, D. C., & Byer, R. L. (1982). Model studies of laser absorption computed tomography for remote air pollution measurement. *Applied optics*, 21(7), 1165-1178.
- Wright, P., Garcia-Stewart, C. A., Carey, S. J., Hindle, F. P., Pegrum, S. H., Colbourne, S. M., & McCann, H. (2005). Toward in-cylinder absorption tomography in a production engine. *Applied optics*, 44(31), 6578-6592.
- Wright, P., Terzija, N., Davidson, J. L., Garcia-Castillo, S., Garcia-Stewart, C., Pegrum, S., & McCann, H. (2010). High-speed chemical species tomography in a multi-cylinder automotive engine. *Chemical Engineering Journal*, 158(1), 2-10.
- Yang, W. Q., Spink, D. M., York, T. A., & McCann, H. (1999). An image-reconstruction algorithm based on Landweber's iteration method for electrical-capacitance tomography. *Measurement Science and Technology*, 10(11), 1065.
- Zdunek, R. (2007). Multigrid regularized image reconstruction for limited-data tomography. *Comp. Meth. Sci. Tech*, 13, 67-77.
- Zhao, H. K., Osher, S., & Fedkiw, R. (2001). Fast surface reconstruction using the level set method. In *Variational and Level Set Methods in Computer Vision, 2001. Proceedings. IEEE Workshop on* (pp. 194-201). IEEE.
- Zhao, S. R., & Halling, H. (1995, October). A new Fourier method for fan beam reconstruction. In *Nuclear Science Symposium and Medical Imaging Conference Record, 1995, 1995 IEEE* (Vol. 2, pp. 1287-1291).